Two-dimensional turbulence cross-correlation functions in the edge of NSTX

S. J. Zweben, D. P. Stotler, F. Scotti, and J. R. Myra

Two-dimensional turbulence cross-correlation functions in the edge of NSTX

S. J. Zweben,[1] D. P. Stotler,[1] F. Scotti,[2] and J. R. Myra[3]
[1]*Princeton Plasma Physics Laboratory, Princeton, New Jersey 08540, USA*
[2]*Lawrence Livermore National Laboratory, Livermore, California 94550, USA*
[3]*Lodestar Research Corporation, Boulder, Colorado 80301, USA*

The 2D radial vs. poloidal cross-correlation functions of edge plasma turbulence were measured near the outer midplane using a gas puff imaging (GPI) diagnostic on NSTX. These correlation functions were evaluated at radii r = 0 cm, ±3 cm, and ±6 cm from the separatrix and poloidal locations p = 0 cm and ±7.5 cm from the GPI poloidal center line for 20 different shots. The ellipticity ε and tilt angle φ of the positive cross-correlation regions and the minimum negative cross-correlation "cmin" and total negative over positive values "neg/pos" were evaluated for each of these cases. The average results over this dataset were $\varepsilon = 2.2 \pm 0.9$, $\varphi = 87° \pm 34°$ (i.e., poloidally oriented), cmin = -0.30 ± 0.15, and neg/pos = 0.25 ± 0.24. Thus, there was a significant variation in these correlation results within this database, with dependences on the location within the image, the magnetic geometry, and the plasma parameters. Possible causes for this variation are discussed, including the misalignment of the GPI view with the local B field line, the magnetic shear of field lines at the edge, the poloidal flow shear of the turbulence, blob-hole correlations, and the neutral density 'shadowing' effect in GPI. *Published by AIP Publishing.*
[http://dx.doi.org/10.1063/1.5002695]

I. INTRODUCTION AND MOTIVATION

Turbulence in magnetized plasmas generally has a two-dimensional filamentary structure with scale lengths parallel to the magnetic field much larger than those across it due to the rapid motion of electrons along a magnetic field line. For example, in tokamaks, the radial and poloidal correlation lengths perpendicular to the magnetic field B are on the order of $\sim$1 cm, while the parallel correlation lengths are normally $\geq$100 cm. An evaluation and understanding of the perpendicular structure of the turbulence can eventually help to explain the turbulent transport of heat and particles through the edge, especially by comparing the experimental results to computational simulations.

This paper describes the 2D structure of the edge turbulence correlation functions as measured by a gas puff imaging (GPI) diagnostic on NSTX, a spherical tokamak. The 2D spatial cross-correlation functions are evaluated in the radial vs. poloidal plane perpendicular to the local magnetic field near the outer midplane separatrix region of NSTX. The ellipticity and tilt angle of the positive cross-correlation regions and the location and magnitude of the negative cross-correlation regions were evaluated at ±6 cm from the separatrix radius and ±7.5 cm from the GPI poloidal center line for 20 different shots. Note that this paper deals only with the "zero-time-delay" spatial cross-correlations (averaged over time) and does not include the analysis of the time-dependent cross-correlations, which determines the turbulence motion. The present analysis does not identify or track isolated or intermittent 'blob' structures in the data but focuses only on the statistical averages over all of the edge turbulence. The structures measured in this experiment cover spatial scales in the range of $\sim$1–20 cm and timescales of $\geq$2.5 μs.

Many previous measurements of edge turbulence have shown that the *average* radial and poloidal correlation lengths in the tokamak edge are typically related by $L_{rad} \sim (0.25–1.0)L_{pol}$.[1] However, there have been relatively few measurements of the full 2D structure of the edge turbulence correlation functions in tokamaks since this requires a turbulence diagnostic with good 2D space and time resolution, such as probe arrays, beam emission spectroscopy (BES), or GPI. Note that the number of spatial points needed to get adequate 2D spatial resolution of the cross-correlation functions has to be at least 4×4, and so, the diagnostic has to have at least 16 nearby spatial channels.

With respect to 2D probe measurements, an 8×8 radial vs. poloidal probe array was used in the Caltech tokamak edge to show that the poloidal correlation length was about $2\times$ larger than the radial correlation length.[2] A limited array of edge probes in DIII-D was able to identify both positive-going and negative-going intermittent events although not their 2D spatial structure.[3] A poloidal array of probes and a separate radial array were used to characterize the 2D SOL turbulence structures in CASTOR.[4] Two 1-D rake probe arrays, one poloidal and one radial, were used in Ohmic plasmas in Tore-Supra to indirectly infer a perpendicular tilting of edge blobs due to the electric field and magnetic shear.[5]

Two-dimensional optical measurements of edge turbulence were made using an 8×8 array of BES detectors in DIII-D,[6] which showed a near-Gaussian radial correlation function, along with a partially wave-like poloidal correlation function. Edge turbulence measurements with both GPI and BES in NSTX have also shown partially wave-like poloidal cross-correlation functions in ELM-free H-mode plasmas.[7,8] Similar BES results have recently been obtained on MAST, including a detailed analysis of the "point spread function," using an outer edge array with 4×4 pixels.[9,10]

Two dimensional GPI turbulence cross-correlation functions have previously been evaluated at Alcator C-Mod,[11] which showed a different correlation tilt with respect to the outer midplane flux surfaces at two different poloidal angles in 64×64 camera images. A highly tilted 2D correlation structure was also seen in the 9×10 APD GPI array in C-Mod, which viewed the gas puff at an angle of $\sim 11°$ to the local B field direction.[12] The 2D correlation functions from GPI cameras above and below the outer midplane in EAST showed tilted structures with angles in opposite directions, as might be induced by magnetic shear.[13] With respect to previous GPI results on NSTX, separate 1-D radial and poloidal correlation lengths were previously evaluated,[14] and the 2D ellipticity and tilt angle of the intermittent blob structures were measured using the same database.[15] A GPI analysis of the 2D turbulence was also done on TEXTOR,[16] showing a stretching and splitting of the turbulence structure with poloidal flow due to electric field biasing. Two dimensional GPI in ASDEX-Upgrade[17] showed similar intermittent blob structures in L-mode and H-mode plasmas.

The present study was also motivated in part by measurements in non-tokamak devices in which the 2D turbulence structure could be measured in more detail. For example, the 2D correlation functions in the LAPD linear device varied significantly during azimuthal rotation induced by electrical biasing,[18,19] and a complex two-dimensional turbulence structure was evaluated in the linear CSDX device using a combination of probes and fast imaging.[20] Detailed cross-correlation measurements in 2D were recently made using probe arrays in the toroidal device TORPEX[21] and the helimak device KT-5D,[22] and two dimensional (poloidal vs. toroidal) probe measurements were made in the TJ-K stellarator.[23]

Finally, an important motivation for this paper is the recent progress in computational simulations of edge turbulence in tokamaks, which are beginning to be validated by edge turbulence measurements.[24–28] Some of these theoretical ideas will be discussed in this paper but without any specific comparisons to simulations for NSTX, which are not yet available.

The outline of this paper is as follows: Sec. II describes the NSTX GPI database used for the present paper, Sec. III describes the alignment of the GPI view, Sec. IV describes the experimental results on the 2D correlation functions, Sec. V has the Discussion, and Sec. VI contains the summary and conclusions.

II. NSTX DATABASE FOR THIS PAPER

The NSTX device is a spherical tokamak with major radius $R_o = 86$ cm, minor radius $a = 65$ cm, and an elongated plasma shape with typically $\kappa \sim 2$.[29] The 20 shots used for the present paper as shown in Table I were chosen to sample the range of magnetic fields and applied heating power within a larger GPI database from the 2010 run.[14,15] The toroidal field range was $B_o = 0.34–0.54$ T (vacuum field measured at R_o), the plasma current range was $I = 0.7–1.1$ MA, and the outer midplane separatrix major radius R_{sep} and stored energy W ranges of Table I were evaluated using magnetic equilibrium derived from EFIT reconstructions (EFIT02). This shot list has a variety of Ohmic, L-mode, and H-mode plasmas but no shots with large MHD activity, ELMs, or L-H transitions during the 10 ms time of GPI analysis. All shots used deuterium fueling with deuterium NBI power from 0 to 6 MW, except one shot with RF (#141984), and all had a lower-single null (or very near single-null) divertor shape.

The turbulence data in this paper were obtained using a gas puff imaging (GPI) diagnostic,[30] which introduces a puff of neutral gas into the plasma edge to increase the local visible light emission for improved space-time resolution of

TABLE I. Shot list for this paper. The angles θ_z and Θ in the right-hand columns are the vertical angle of the magnetic field at the target plate and the magnitude of the magnetic field misalignment at the central grid point (r,p) = (0,0).

	Shot	Time (s)	Type	B_0(T)	I(MA)	I/B	R_{sep} (cm)	P_{aux} (MW)	W (MJ)	θ_z (deg)	Θ (deg)
1	138122	0.230	OH	0.44	0.93	2.10	148	0.0	35.0	27.8	10.1
2	138126	0.245	OH	0.44	0.93	2.10	148	0.0	41.7	29.2	8.8
3	138844	0.615	H	0.44	0.82	1.86	151	3.8	215	38.9	5.9
4	138848	0.615	H	0.44	1.0	2.31	148	3.8	259	42.7	7.9
5	139045	0.415	H	0.49	1.0	2.10	150	5.9	244	38.5	6.2
6	139050	0.415	H	0.54	1.1	2.09	149	6.0	307	37.4	6.0
7	139289	0.315	H	0.49	0.83	1.69	149	3.0	133	32.2	9.0
8	139442	0.290	L	0.54	1.1	2.10	148	2.0	113	32.9	8.9
9	139444	0.265	OH	0.34	0.68	1.98	148	0.0	47.2	33.2	8.6
10	139446	0.225	OH	0.34	0.71	2.06	148	0.0	34.7	31.7	8.1
11	139501	0.515	H	0.47	0.92	1.95	147	2.0	164	35.5	7.0
12	139951	0.365	H	0.44	0.94	2.11	147	5.0	219	39.4	7.3
13	140392	0.545	H	0.49	0.84	1.70	146	4.0	223	36.4	8.6
14	140623	0.265	H	0.47	0.94	1.98	148	1.9	130	32.8	9.7
15	141270	0.475	H	0.44	1.0	2.33	146	3.8	221	39.5	8.6
16	141741	0.215	OH	0.41	0.72	1.79	149	0.0	26.5	26.0	11.8
17	141912	0.285	OH	0.44	0.91	2.05	152	0.0	53.4	30.4	6.1
18	141984	0.230	L	0.44	0.93	2.09	154	1.1 (RF)	57.1	30.7	5.1
19	142220	0.285	L	0.44	0.81	1.83	149	0.96	69.2	31.4	8.5
20	142270	0.375	L	0.44	0.81	1.82	151	1.0	66.7	32.1	6.3

plasma fluctuations. For the present paper, the GPI gas puff was deuterium, and the fluctuations were imaged using neutral Dα light emission. As discussed in Ref. 30, these Dα light emission fluctuations can be due to either electron density or electron temperature fluctuations, but the spatial cross-correlation functions of the Dα light emission (as calculated in this paper) should be independent of the details of these dependencies if these density and temperature fluctuations are cross-correlated with each other.

In the previous NSTX GPI database, the edge field line angle was constrained using an approximate criterion $I/B_o = 2.0 \pm 0.5$ MA/T, but for the present study, the edge magnetic field line angles were more precisely calculated using the local B fields from EFIT reconstructions. For all shots described in this paper, the GPI gas puff source was D$_2$ at room temperature, and the time of analysis was within ± 5 ms of the peak of the GPI gas puff rate in each shot (as in the analysis of the larger database). The 2D cross-correlation patterns were quite reproducible for shots with similar plasma parameters.

III. ALIGNMENT OF THE GPI VIEW

In order to properly interpret the 2D cross-correlation functions in GPI over the plane of the GPI images, it is necessary to understand the diagnostic geometry. The most significant issue is the alignment between the GPI viewing angle and the local magnetic field direction, which was previously assumed to be aligned close enough so as to not significantly affect the calculated turbulence correlation lengths.[14,15] These geometrical misalignments between the GPI viewing angle and the local B field can affect the GPI spatial resolution due to the finite size of the GPI light emission cloud. In this section, we examine the effects of an angular misalignment more carefully and estimate how much this affects the 1-D cross-correlation functions, given the estimated size of the turbulence itself and of the GPI emission cloud. The 2D cross-correlation functions will then be described in detail in Sec. IV.

A. GPI hardware geometry in NSTX

In Fig. 1(a) is a cross section of a typical NSTX plasma in the major radial vs. vertical plane, showing the projection of the GPI field of view just above the outer midplane and the GPI gas puff manifold as a green line. In Fig. 1(b) is a photograph of the GPI hardware inside the vessel, which shows the GPI gas puff manifold attached to the outer wall ~ 20 cm above the midplane and a few cm radially behind the shadow of the downstream RF antenna limiter. The GPI gas cloud was created by a linear array of thirty 1 mm diameter holes located 1 cm apart on this manifold, which was installed approximately perpendicular to the edge magnetic field lines B. The GPI optical view is indicated by the yellow arrow with the optical vertex to the right and with a B field line illustrated schematically in orange.

The GPI hardware geometry was calibrated during a machine opening using an in-vessel target plate attached to the GPI gas manifold to simulate the plane of the light-emitting object formed by the GPI gas cloud, as shown in blue in Fig. 1(b). This target plate was aligned with the holes of the manifold and perpendicular to the local vessel toroidal wall. The GPI camera viewing region was aligned (as closely as possible) so that the camera image of the target plate was oriented with the local minor (not major) radial direction horizontal and the local poloidal (i.e., "binormal") direction vertical, i.e., in the plane perpendicular to the local magnetic field. The GPI hardware coordinates are summarized in Table II, including the center of the GPI camera image at pixel (32,40) and the vertex of the optical view (after removing the mirror reflection). This GPI optical view was the same for all shots in the 2010 run even though the local magnetic field direction varied for different plasmas.

Typical GPI images using this view are illustrated in Fig. 2, where the separatrix is shown by the dashed line, the RF limiter shadow by the dotted line, and the GPI gas manifold position by the white line at the right. These images show the Dα light intensity (raw camera data) over the camera's full 64×80 pixel range, covering an area of approximately 24 cm radially (horizontally) $\times$ 30 cm poloidally (vertically), taken with an exposure time of ~ 2.1 μs near the time of the peak GPI puff rate at a framing rate of $\sim 400\,000$ frames/s. The shot in Fig. 2(a) had a relatively small separatrix radius $R_{sep} = 148$ cm (#139442), and the shot in Fig. 2(b) had a larger $R_{sep} = 152$ cm (#141912), illustrating how the radial profile of GPI light emission moves with the separatrix position since it depends on the edge plasma parameters. The
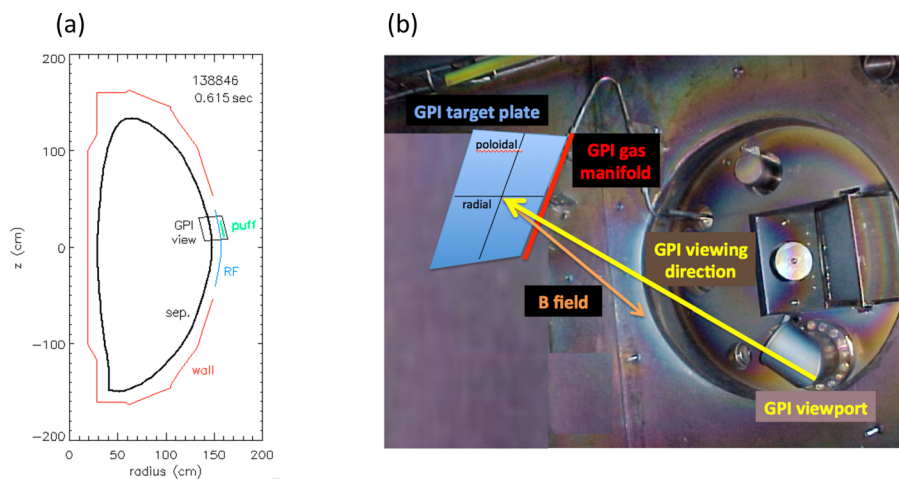
(a)   (b)

FIG. 1. GPI geometry in NSTX. (a) A cross section of a typical NSTX plasma in the radial vs. vertical plane (R,z), showing the trapezoidal GPI field of view just above the outer midplane and the GPI gas puff manifold as a green line. (b) Photo of the GPI hardware inside the vessel, with the GPI gas puff manifold attached to the outer wall ~ 20 cm above the outer midplane. The GPI optical view is shown by the yellow arrow with the optical vertex at the right, with a B field line shown schematically in orange, and with the optical calibration target plate in blue (attached to the manifold).

TABLE II. GPI geometry in NSTX.

	R (cm)	z (cm)	Toroidal angle (deg)
Optical vertex @ lens	170.2	−21.4	43
Image center @ (32,40)	149.1	19.9	62
Distance from the optical vertex to the image center = 69 cm			
Vertical angle of the GPI view @ the image center (32,40) = 36.8°			

shot times for these frames are shown below the shot numbers (e.g., 0.285025 s).

The 5×3 grid of crosses in Fig. 2 show the origin points of the 2D correlation functions to be analyzed in this paper, which are located at radii r = ±6 cm, ±3, and 0 cm with respect to the separatrix for each shot (defined at the vertical middle row #40) and at poloidal locations p = ±7.5 and 0 cm with respect to the vertical middle. Origin points vertically outside this grid are too close to the edges of the image to contain the 2D correlation functions, and points farther outside than r = +6 cm with respect to the separatrix have GPI signal levels which are too low to use. The innermost radial locations at r = −6 cm are sometimes too close to the left edge of the image to define a complete cross-correlation function, as in Fig. 2(a). Note that the separatrix at the poloidal locations p = ±7.5 cm can deviate by up to ∼1–2 cm from its location at p = 0 cm in these images, but for this analysis, the local poloidal direction will be taken as vertical and the local radial direction as horizontal. The separatrix location based on EFIT02 is uncertain by ±1–2 cm.

The spatial calibration data for the GPI target plane and camera view were incorporated into a GPI alignment code along with the magnetic equilibrium for each shot. The angles between the viewing chords (i.e., from the optical vertex to each camera pixel) and the local magnetic field direction at each pixel were calculated in the GPI target plane. A

sample plot of the result is shown in Fig. 3(a), where the contour lines show the *magnitude* of the angle between the GPI viewing chord and the local B field (in degrees), and the arrows indicate the relative magnitude and direction of the target plane component of the vector differences between the viewing chords and the magnetic field. The axis coordinates here are in pixels corresponding to the images in Fig. 2, the dark red horizontal dashed line is the vertical center of this image (row #40), and the dark red vertical dashed line is the separatrix location at the vertical center. Other dashed lines are also shown at radial locations r = ±3 cm and ±6 cm from the separatrix and poloidal locations p = ±7.5 cm from the vertical center, which define the 15 grid points shown in Fig. 2.

The shot in Fig. 3(a) has a near-perfect poloidal viewing angle at a vertical B field line angle $\theta_z = \operatorname{atan}(B_z/B_{tor})$ = 36.4° (see Table I); however, this perfect alignment point was at a horizontal pixel #46/64, which was 10.5 cm radially outside the separatrix. Using from now on the image coordinate notation (r,p), for example, (0,0), to mean the grid point at r = 0 cm and p = 0 cm in the 5×3 grid of Fig. 2, the *magnitude* of the B field misalignment for this shot is $\Theta \sim 8.6°$ at (0,0), and the *direction* of this misalignment was $\Phi \sim 167°$, as measured counterclockwise from the horizontal (i.e., radially outward) direction in this plot. The range of B field misalignment angles over the 5×3 grid for this shot was $\Theta \sim 3.8°–19.6°$, with the best alignments for the largest radial grid points. In general, an offset of 20 cm from the point of perfect alignment with B in the GPI target plane corresponds to a misalignment angle in the GPI target plane of $\Theta \sim 16°$.

Figures 3(b)–3(d) show B field angle alignment maps like that of Fig. 3(a) for three other shots. In Fig. 3(b), the perfect alignment is near the bottom of the image for this
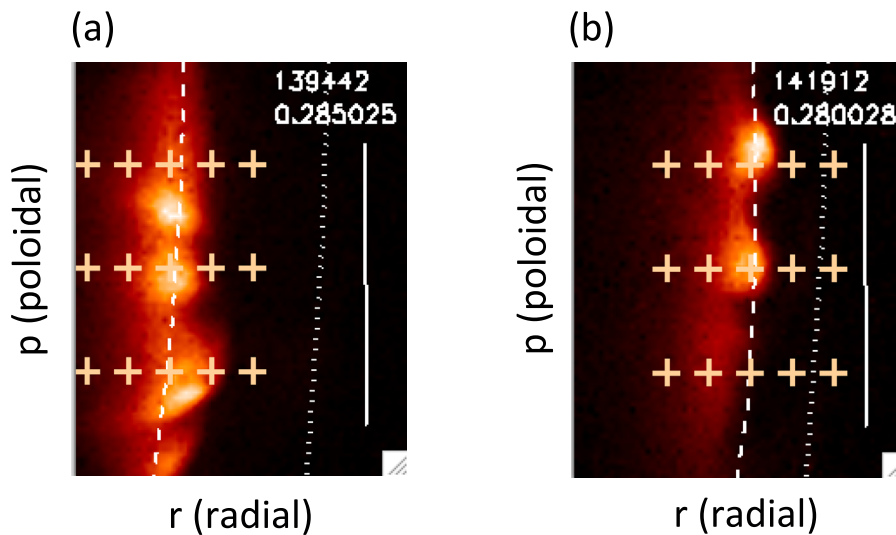
(a)   (b)

FIG. 2. Typical GPI images from single frames for two shots, in which the Dα light intensity is shown by a false color scale with white as maximum and black as zero. The separatrix is shown by the dashed line, the RF limiter shadow by the dotted line, and the GPI gas manifold by the white line at the right. The local minor radial direction is nearly horizontal, and the local poloidal (i.e., binormal) direction is nearly vertical. The scale is ∼24 cm radial × 30 cm poloidal. Shot (a) had the separatrix relatively far inward (#139442), and shot (b) had a separatrix ∼4.5 cm farther outward (#141912), showing how the GPI light emission moves radially with the separatrix. The 5×3 array of points used for analysis are shown by the crosses, which are located at radii r = ±6 cm, ±3, and 0 cm with respect to the separatrix and p = ±7.5 and 0 cm with respect to the middle of the poloidal range of the images. The shot times for these frames are shown below the shot numbers (e.g., 0.285025 s).
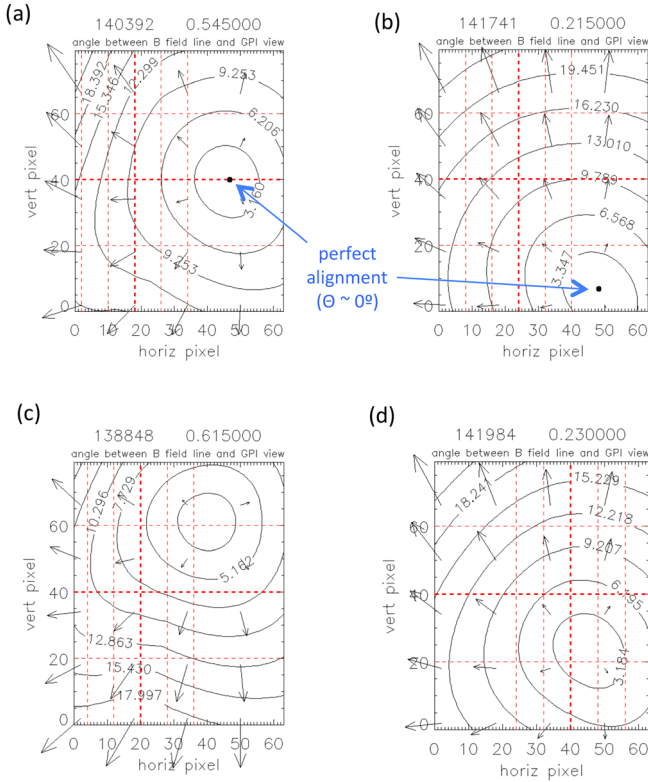
FIG. 3. (a) The calculated angles between the local B field line and the GPI view in the image plane for a shot with near perfect vertical alignment at the poloidal center of the image (#140392). The axis coordinates are in pixels, corresponding to the images shown in Fig. 2. The contour lines show the magnitude of the misalignment angle in degrees, and the arrows show the direction and relative magnitudes of the B field misalignment at various points. The vertical dashed lines are at the separatrix location at the poloidal center of the image and radial locations $r = \pm 3$ cm and ± 6 cm from this separatrix, and horizontal dashed lines are at poloidal locations $p = 0$ cm and ± 7.5 cm from the vertical center. Parts (b)–(d) show similar maps for three other shots. The optimal B field alignment is near the top of the GPI image in (b) and near the bottom of the image in (c), corresponding to extremes in vertical B field angles θ_z (see Table I). The shot in (d) has the lowest misalignment angles at the separatrix, corresponding to the shot with the largest separatrix radius of Table II. The directions of the misalignment vary considerably with the position within the images, as shown by the arrows.

shot, which had the smallest vertical field line angle $\theta_z = 26°$ (#141741). The perfect alignment in Fig. 3(c) is near the top of the image for this shot with the highest vertical field line angle of $\theta_z = 42.7°$ (#138848). The shot in Fig. 3(d) has the largest separatrix radius R_{sep} in Table I (bold vertical dashed red line), resulting in a better alignment at the separatrix location compared to the shot of Fig. 3(a) which had (nearly) the smallest R_{sep}. The magnitude of the B field misalignment at grid point (0,0) for each shot is given in the last column of Table I; these misalignment angles are in the range of $\Theta \sim 5°$–$12°$, and the average value is $\Theta \sim 8°$.

Since the major radii of all points in the GPI image plane are less than the optical vertex at $R = 170.3$ cm (Table II), all points in the image plane are also angled radially inward with respect to the viewing direction but in the same way for all shots. This angle is taken into account in the misalignment calculations shown in Fig. 3.

The B field alignment angle magnitudes Θ and directions Φ were calculated for all 20 shots at all 15 grid points,

i.e., at radial locations $r = 0$ cm, ± 3 cm, and ± 6 cm from the separatrix and vertical locations $p = 0$ cm and ± 7.5 cm from the vertical center (see Fig. 2). The largest misalignment magnitude was $\Theta \sim 20.3°$ for the $(r,p) = (-6$ cm, 7.5 cm) grid point of shot #141741, and the best alignment was $\Theta \sim 1.2°$ for the $(+6$ cm, -7.5 cm) grid point of shot #141912. The magnitude of the misalignment over the database varied across the GPI image plane, increasing from an average of $\Theta \sim 6°$ at $+6$ cm outside the separatrix to $\Theta \sim 13°$ at -6 cm inside the separatrix and from $\Theta \sim 8°$ at $p = -7.5$ cm to $\Theta \sim 11°$ at $p = +7.5$ cm. The *direction* of the misalignment angle Φ varies widely within the image plane, as illustrated in Fig. 3.

B. GPI emission cloud geometry

These geometrical misalignments between the GPI viewing angle and the local B field can affect the GPI spatial resolution due to the finite size of the GPI light emission cloud. This is illustrated schematically in Fig. 4, where for simplicity in this discussion, the turbulence filament is assumed to have a circular cross-section aligned along B and to emit light only within the GPI cloud.

Figure 4(a) shows a top-down view of the plane of the local B field line, with the GPI emission cloud in green and the target plane of Sec. III A shown as a blue line. Since the length of the GPI viewing chord within the cloud is small compared to the plasma major radius of $R \sim 150$ cm at this location (see below), the local B field line is assumed to be straight but with a misalignment angle Θ with respect to the GPI viewing chord, as shown in the oblique view of Fig. 4(b). Figure 4(c) shows how this turbulence filament within the cloud looks from along the GPI viewing chord near the image plane. Instead of a circular filament cross-section, which would be obtained with perfect alignment $\Theta = 0$, the turbulence filament will appear to be extended along the direction of the misalignment by a distance $\delta \sim L_{II} \tan \Theta$, at least for small Θ. If this distance is comparable to or larger than the filament diameter, then the spatial resolution of the turbulence filament will be affected, along with the measured turbulence correlation functions.

The parallel length L_{II} of the GPI emission cloud along B was not directly measured in these experiments. However, since the gas manifold holes were not highly collimated, the GPI neutral gas should have an approximate cosine angular distribution,[31] i.e., with a length along the B field line roughly the same as the distance from the manifold hole, which is in the range of ~ 10–15 cm in the center of the GPI image (see Fig. 2). A better estimate was made using the DEGAS 2 neutral transport code, which has previously been used to simulate the 2D emission pattern in the GPI image.[32] The FWHM of the emission cloud from DEGAS 2 is shown in Fig. 5 to be $L_{II} \sim 12$ cm, roughly independent of the radius within ± 10 cm of the separatrix and independent of time during the GPI gas puff. Since there was no significant dependence of this FWHM on the vertical pixel coordinate, the results shown in Fig. 5 were averaged over this coordinate.

Using this estimate of the cloud length $L_{II} \sim 12$ cm and an average misalignment near the separatrix of $\Theta \sim 8°$ at the
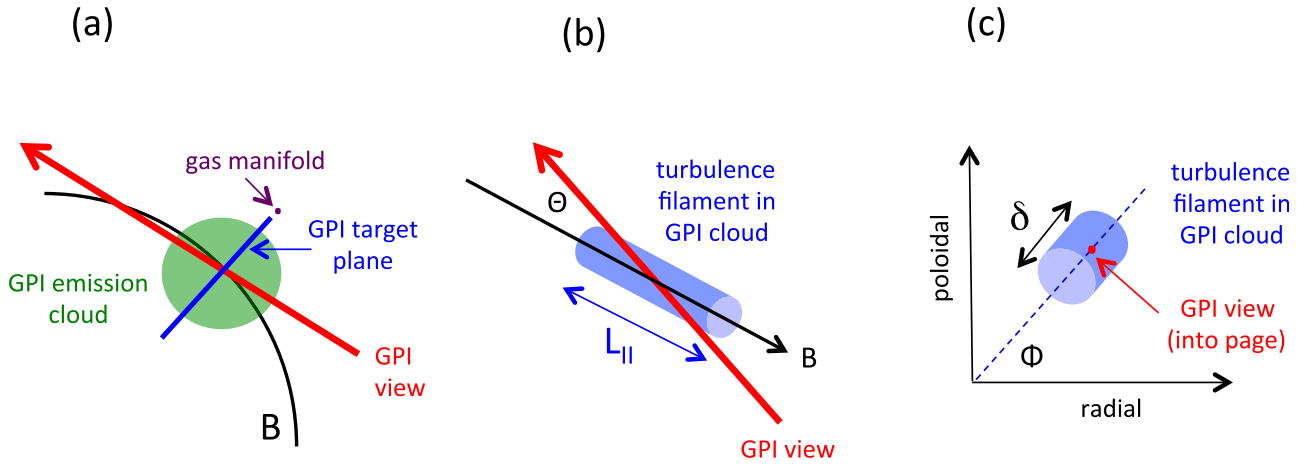
FIG. 4. (a) A top-down view in the B field line plane, with the GPI emission cloud in green and the target plane of Sec. III A shown as a blue line. (b) An oblique view with the parallel emission length of the cloud L_{II} and the local B field at a misalignment angle of Θ to the GPI view. (c) View from the GPI vertex direction, showing the "smearing" of the turbulence filament by a length δ in the direction of the misalignment angle Φ.

vertical center (Table I), the average "smearing" distance of the turbulent filament is $\delta \sim L_{II} \tan \Theta \sim 1.7$ cm. This is generally small compared with the GPI-measured radial and poloidal correlation lengths of the turbulence of $L_{pol} \sim L_{rad} \geq 5$ cm (FWHM), as discussed further in Sec. III C, so this smearing should not significantly affect the measured correlation lengths. Note that there is actually a small range of misalignment angles for a given viewing sightline due to the finite length of the cloud along B. A cloud length of $L_{II} \sim 12$ cm has a total angular displacement of $\sim 4.5^\circ$ along the field line, which implies an additional variation in the B field alignment angle of about $\pm 2.3^\circ$ (out of 8°). For example, this adds an uncertainty to the calculated smearing

length of $\delta \sim L_{II} \tan \Theta \sim 1.7 \pm 0.5$ cm for the case above, which does not significantly affect the prior conclusion.

C. Misalignment effects on 1-D correlation lengths

Before proceeding to discuss the full 2D correlation functions in Sec. IV, we re-evaluate the effects of the GPI viewing misalignment on previous analyses of the 1-D poloidal and radial correlation lengths, which assumed perfect alignment. Those correlation lengths were evaluated only at the vertical middle of the images over a range of -2 cm inside to $+4$ cm outside the separatrix, using the normalized 2-point cross-correlation coefficients at a separation of 2.4 cm, assuming a Gaussian cross-correlation coefficient.[14]

Figure 6(a) shows a reanalysis of 1-D correlation lengths for the present database. In Fig. 6(a) are the calculated smearing lengths $\delta \sim L_{II} \tan \Theta$ in the direction of the local B field misalignment for each point on the 5×3 spatial grid of Fig. 2 for each shot, i.e., at radial distances $r = 0$ cm, ± 3 cm, and ± 6 cm from the separatrix and $p = 0$ cm and ± 7.5 cm poloidally from the middle of the GPI images. The average (black line) runs from $\delta = 2.8 \pm 0.7$ cm at a radius of -6 cm to $\delta = 1.3 \pm 0.7$ cm at a radius of $+6$ cm (results for $p = +7.5$ cm are $\sim 20\%$ higher than those for $p = 0$ and -7.5 cm). These smearing effects due to the misalignment and cloud geometry are larger than the optical resolution at the target plane of ~ 0.5 cm and the pixel size of ~ 0.4 cm and so are the main limiting factors in the spatial resolution of the GPI for these data.

Figure 6(b) shows the 1-D correlation lengths calculated for these same points using the 2-point method of Ref. 14, still assuming perfect field line alignment. The average results as shown by the linear fits are similar to those found previously,[14] i.e., $L_{pol} \sim 6.3 \pm 1.9$ and $L_{rad} \sim 5.0 \pm 2.1$ cm (FWHM). Note that these data represent a wide range of plasma parameters in NSTX, including Ohmic and H-mode plasmas (see Table I). A separate evaluation of these correlation lengths using the complete 1D cross-correlation functions (when possible given the spatial limits of these images) gave FWHM correlation lengths of 1.1 ± 0.2 times larger
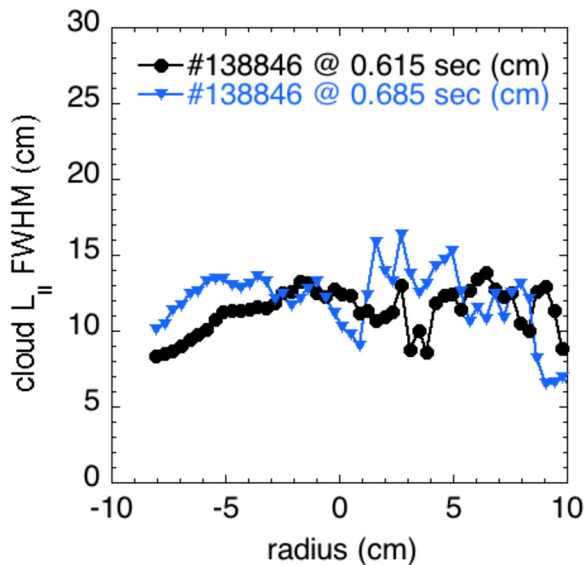

FIG. 5. DEGAS 2 calculation of the length of the GPI emission cloud L_{II} (FWHM) along the magnetic field direction vs. the radial distance from the separatrix within the GPI image, based on simulations in Ref. 7. The result is $L_{II} \sim 12$ cm, roughly independent of the radius within ± 10 cm of the separatrix and of time during the gas puff. There was no significant dependence of this FWHM on the vertical pixel coordinate, so the results of were averaged over this coordinate.
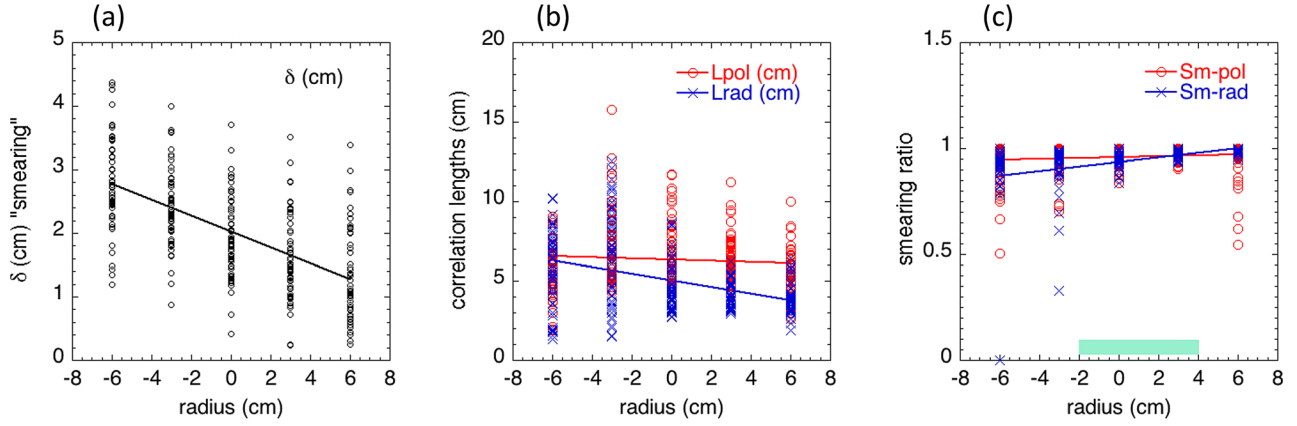
FIG. 6. Effects of geometrical smearing on the 1-D correlation lengths for the 5×3 spatial grid for the shots of Table I. (a) The total length δ of the estimated smearing in the direction of the B field misalignment vs. distance from the separatrix location. (b) The measured poloidal and radial correlation lengths for these points. (c) The estimated relative effects of this smearing on these correlation lengths. The green bar shows the radial region used in the previous analysis.[14]

than these 2-point estimates for L_{pol} and 0.74 ± 0.26 times larger than these 2-point estimates for L_{rad}, suggesting that the correlation functions are not Gaussian, particularly in the radial direction, as discussed further in Sec. IV F.

To estimate the B field misalignment effects on the 1-D correlation lengths, the smearing lengths in the poloidal (i.e., vertical) and radial (i.e., horizontal) directions were obtained from the calculated directional smearing lengths δ of Fig. 6(a) by using the local B field misalignment directions, i.e., $\delta_{pol} = \delta \sin \Phi$ and $\delta_{rad} = \delta \cos \Phi$, where Φ is the calculated misalignment direction measured counter-clockwise from the horizontal (outward). The measured correlation lengths presumably include these smearing lengths, which were generally smaller than the correlation lengths, i.e., $\delta_{pol}/L_{pol} \sim 0.22 \pm 0.17$ and $\delta_{rad}/L_{rad} \sim 0.28 \pm 0.20$. The approximate effect of this smearing on the measured 1-D correlation lengths was then evaluated as the "smearing ratios": $Sm_{pol} \sim \sqrt{(L_{pol}^2 - \delta_y^2)/L_{pol}}$ and $Sm_{rad} \sim \sqrt{(L_{rad}^2 - \delta_x^2)/L_{rad}}$. These ratios are shown in Fig. 6(c) for the same data points as in Figs. 6(a) and 6(b) along with linear fits and give the approximate correction factor needed to obtain the actual correlation lengths from the measured correlation lengths, given the smearing due to misalignment.

These correction factors averaged over the whole database were $Sm_{pol} = 0.96$ and $Sm_{rad} = 0.94$, indicating that the relative effects of misalignment on the 1-D correlation lengths were generally $\leq 10\%$ within this spatial grid although there were $\sim 20/300$ points with Sm ratios ≤ 0.8 at radial locations of -3 cm and ± 6 cm from the separatrix. These extreme radial locations were not used in the previous analysis of correlation lengths,[14] which were analyzed only at $p = 0$ from -2 cm inside to 4 cm outside the separatrix (green bar), where the average correction ratios were $Sm_{pol} = 0.97$ and $Sm_{rad} = 0.95$.

In summary, the calculated effects of B field misalignment on the measured 1-D correlation lengths in these GPI experiments were generally $\leq 10\%$. However, the effects of this misalignment on the 2D tilt of the correlation functions can be larger, as discussed in Sec. IV. It should also be noted that these effects were based on the *calculated* GPI gas puff cloud length along B and so are subject to possible revision based on future measurements of the cloud size.

IV. EXPERIMENTAL RESULTS ON 2D CORRELATION FUNCTIONS

This section describes the 2D GPI cross-correlation data analysis and results using the shots from Table I. The cross-correlation function $C(\mathbf{x}_1, \mathbf{x}_2)$ is defined as follows:

$$C(\mathbf{x}_1, \mathbf{x}_2) = \langle [S_i(\mathbf{x}_1) - \langle S_i(\mathbf{x}_1)\rangle] [S_i(\mathbf{x}_2) - \langle S_i(\mathbf{x}_2)\rangle] \rangle /$$
$$\left\{ \langle [S_i(\mathbf{x}_1) - \langle S_i(\mathbf{x}_1)\rangle]^2 [S_i(\mathbf{x}_2) - \langle S_i(\mathbf{x}_2)\rangle]^2 \rangle \right\}^{1/2}$$

$$(1)$$

where the time series over the index "i" are from two pixels $\mathbf{x}_1$ (the origin pixel in the 2D plane) and $\mathbf{x}_2$ (a variable pixel in the 2D plane) within the 2D GPI images (see Fig. 2), with the sum, indicated by the angle brackets, extending over $i = 3976$ frames covering 10 ms. This cross-correlation coefficient C is normalized to lie between $C = -1.0$ and $+1.0$, with $C = +1$, indicating that the two pixels are perfectly correlated to each other with the same sign, $C = -1$, indicating that the two pixels are perfectly correlated to each other but with the opposite sign, and $C \sim 0$, indicating that the two pixels largely uncorrelated over this time series. Qualitatively, the region of positive correlation $C \geq 0.5$ is the spatial region over which the fluctuations are similar to those at a given point, and the region of negative correlation $C < -0.5$ is where fluctuations are similar but of opposite sign with respect to the origin point. There is always a small random correlation for unrelated signals, typically $C \leq 2\%$ for 3976 points.

Note that the average values of each time series are subtracted before C is calculated and that the results are then normalized by both signals so that the magnitude of the GPI light emission (which is in part determined by the GPI gas cloud shape) does not affect the cross-correlation coefficients. Note also that no time lags are imposed on these time series, so these correlations are all for "zero time-delay" and so describe only the instantaneous spatial structure of the correlation functions and not the time dependences, which define the turbulence motion. The turbulence motion is of course an interesting subject but beyond the scope of the present analysis.

Section IV A gives an overview of the 2D correlation results using a few specific examples, Sec. IV B describes the cross-correlation analysis, Sec. IV C describes the database of cross-correlations, Sec. IV D discusses variations in these

correlations with plasma parameters, Sec. IV E discusses the negative regions of the cross-correlation functions, and Sec. IV F describes the 1-D shapes of the cross-correlation functions. Theoretical interpretations are deferred to Sec. V.

A. Examples of 2D correlation functions

Figure 7 shows two examples of the 2D cross-correlation functions for the shots used in Fig. 3, namely,

140392 [Figs. 3(a)] and 141984 [Figs. 3(d)]. For each shot, the 2D cross-correlation functions $C(\mathbf{x}_1,\mathbf{x}_2)$ are plotted over the 64×80 pixel (24×30 cm) image for origin points $\mathbf{x}_1$ located at 15 different grid points corresponding to radial positions $r = 0$ cm, ± 3 cm, and ± 6 cm with respect to the separatrix and poloidal positions $p = 0$ cm and ± 7.5 cm with respect to the vertical middle of the images. These grid points are ordered in Fig. 7 from a low to high radius from
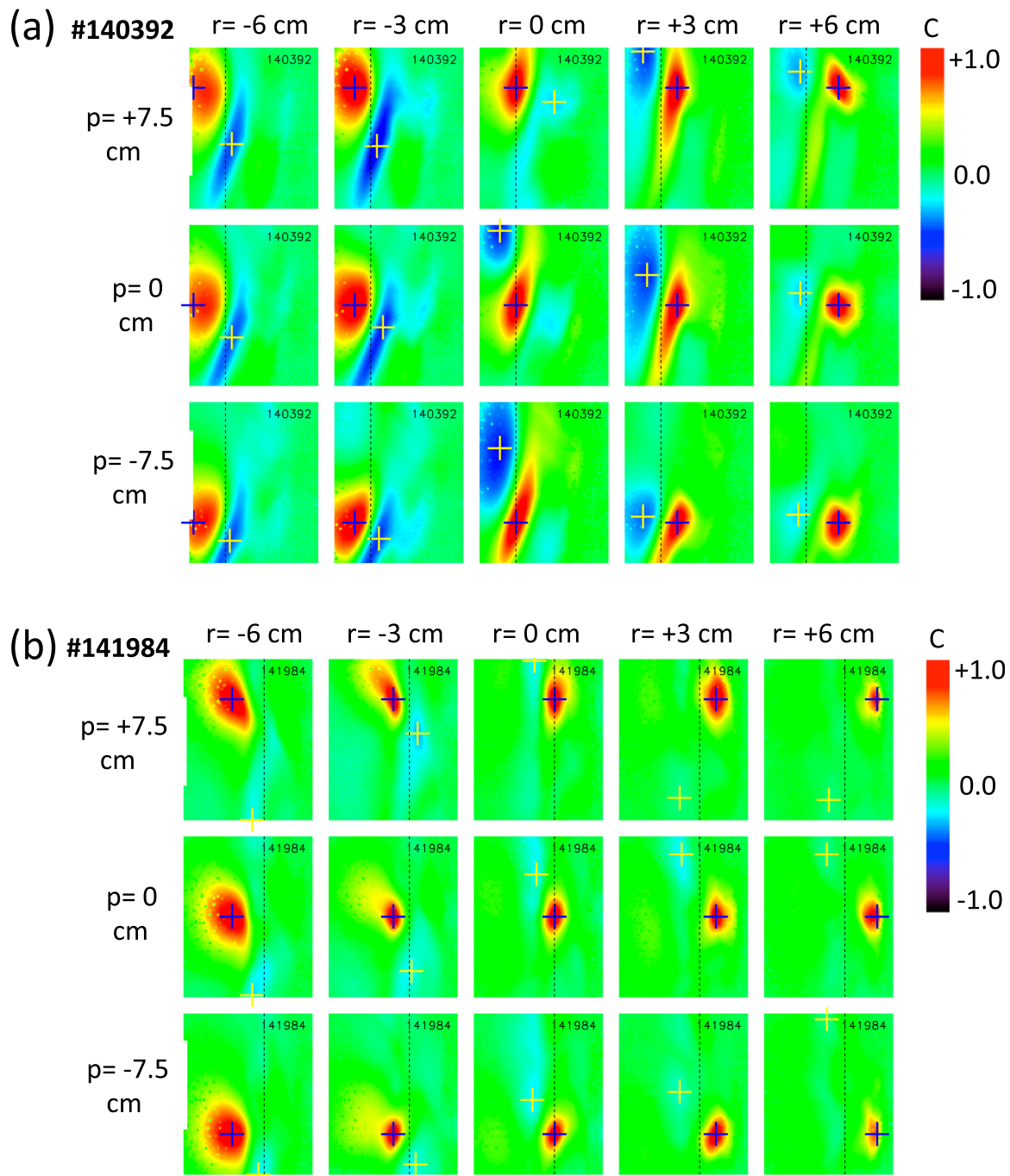

FIG. 7. The 2D cross-correlation functions for two shots used in Fig. 3, namely, (a) #140392 and (d) #141984. For each shot, the cross-correlation functions are plotted over the 64×80 pixel (24×30 cm) image on a 5×3 spatial grid, corresponding to radial positions $r = 0$ cm, ± 3 cm, and ± 6 cm with respect to the separatrix and $p = 0$ cm and ± 7.5 cm with respect to the poloidal center of the images. The correlation color map ranging from -1 to $+1$ is shown at the right. The separatrix location (at the vertical middle) is shown by the dashed lines. The origin pixel for each plot is shown by the blue "+," at which the cross-correlation function has a value of $C = +1$ in all cases, and a correlation of $C = 0.5$ is shown in yellow. The dark blue regions indicate $C \sim -0.5$, and the yellow crosses show the minimum negative cross-correlation in each image.

left-to-right and from a low to high poloidal location from bottom-to-top, and in the same way, these points are arranged in the actual images.

The cross-correlation color map amplitude in Fig. 7 is from −1 (black) to +1 (red), as shown at the right, and the separatrix location at the vertical midplane is shown by the dashed lines. The origin pixel for each plot is shown by the blue "+," at which the cross-correlation function has a value of C = +1, and the yellow "+" shows the location of the maximum negative cross-correlation in each image. The half-maximum points near C = 0.5 are yellow in color, the green indicates C ∼ 0, where there is little or no correlation with the origin point, and the dark blue color indicates C ∼ −0.5, i.e., points which are fairly well correlated with the origin point but with the opposite sign.

Shot #140392 in Fig. 7(a) had near-perfect poloidal alignment of the GPI viewing angle, as shown in Fig. 3(a). The red regions of high positive cross-correlation were near-circular for radii at r = −6 cm, −3 cm, and +6 cm but were quite poloidally elongated at r = 0 cm and +3 cm, with a relatively little variation in shape over the three vertical positions. The average correlation lengths for all 15 grid points were $L_{pol} \sim 8.3$ cm and $L_{rad} \sim 5.6$ cm at FWHM. Perhaps the most striking features of this shot are the large negative correlation regions (blue), which have minimum values near

C ∼ −0.5 for most of the 15 grid points in this 2D analysis. Very similar 2D correlation maps were obtained for similar H-mode shots #140393–395 in this series, and the 2D correlation maps were also very similar among a series of similar Ohmic shots #138121–138124 (not shown).

Shot #141984 in Fig. 7(b) had the largest separatrix radius in this shot list, corresponding to the field alignment map in Fig. 3(d), with perfect alignment at radius r = +2 cm and poloidal position p ∼ −5 cm. The red regions of high positive cross-correlation were near-circular for this shot, with average correlation lengths of $L_{pol} \sim 6.5$ cm and $L_{rad} \sim 3.9$ cm FWHM. The correlation lengths were the largest at the smallest radius of −6 cm and smallest at the largest radius of +6 cm but showed no significant variation with the poloidal position. The negative correlation regions were relatively weak in this shot, compared to those in Fig. 7(a), with an average minimum correlation coefficient of −0.17 over all 15 grid points.

Two other examples of 2D cross-correlation functions are shown in Figs. 8(a) and 8(b). These are from the shots in which the poloidal B field misalignment was the largest in either direction, as shown in Figs. 3(b) and 3(c), with the best alignment near the bottom of the GPI image in Fig. 8(a) and near the top of the image in Fig. 8(b). For these two cases, the cross-correlation function tilt angles φ appear
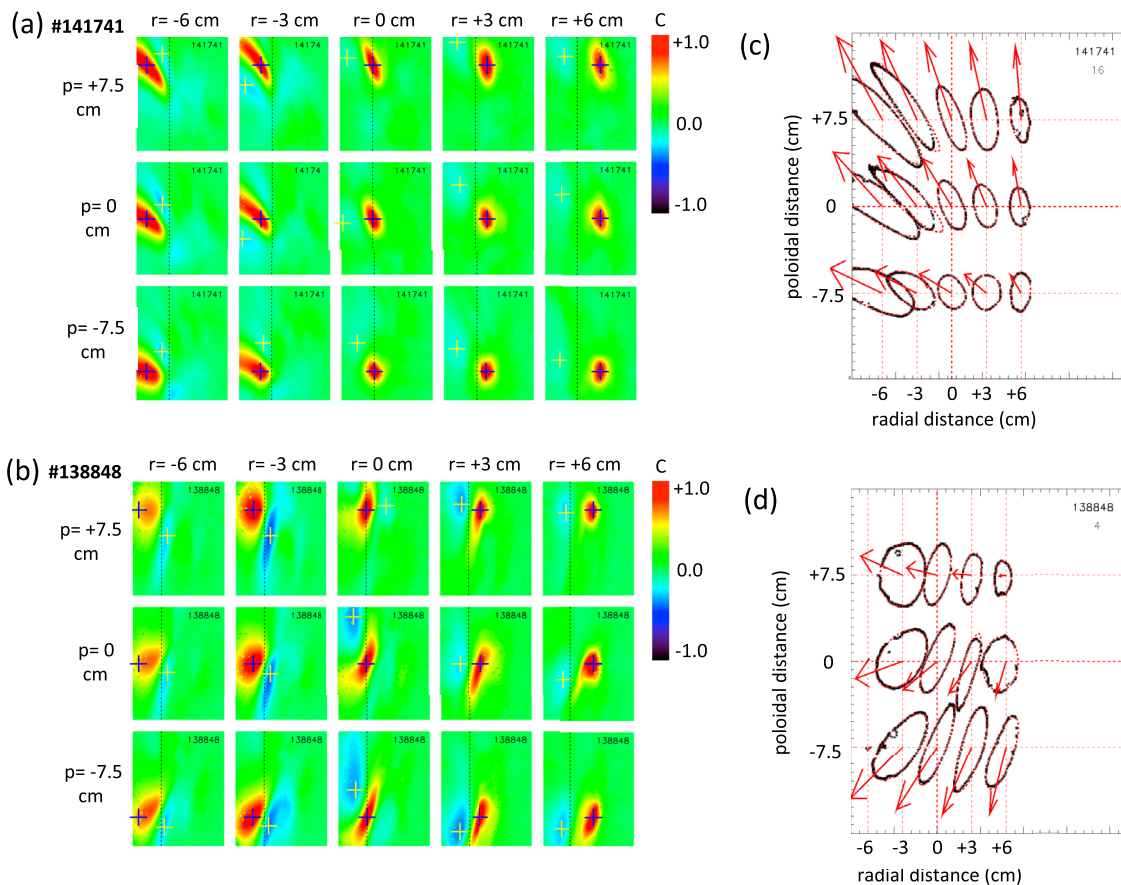

FIG. 8. Further examples of the 2D cross-correlation functions for shots (a) #141741 and (b) #138848, which have the most extreme B field misalignment (see Fig. 3). Parts (c) and (d) show the ellipse fits at C = 0.8 near the origin of each grid point, along with the corresponding misalignment angle magnitudes and direction. The tilt of the correlation functions nearly matches the direction of B field misalignment when the misalignment magnitudes (length of arrows) are the largest.

systematically different, with most cases having tilt angles φ > 90° in Fig. 8(a) and φ < 90° in Fig. 8(b), as measured counterclockwise with respect to the outward radial direction. This suggests that the B field misalignment affects the measured tilt angles, at least for these shots with the largest misalignment angles in this database.

B. Analysis of 2D the correlation functions

The examples in Figs. 7 and 8 suggest the following questions: (1) what determines the tilt angle and ellipticity of the positive (red) regions of the cross-correlation functions, (2) what determines the magnitude and the location(s) of the negative (blue) regions of the cross-correlation functions, and (3) are the correlation function shapes Gaussian? These questions will be answered experimentally in the remainder of Sec. IV, and the results are discussed from a theoretical perspective in Sec. V.

From the normalized cross-correlation function maps such as shown in Figs. 7 and 8, the following quantities were calculated for each of the 5×3 grid points for each shot: the ellipticity ε (i.e., major axis/minor axis) and tilt angle φ (measured counterclockwise with respect to the outward radial direction) of the positive part of the 2D correlation function, the magnitude and location of the most negative cross-correlation points, the average relative magnitudes of the negative/positive correlation regions, and the 1-D radial and poloidal shapes of the correlation functions.

To define the positive cross-correlation region shapes, each 2D cross-correlation function was fit to an ellipse defined by the points at $C = 0.8 \pm 0.005$ on an interpolated (sub-pixel) grid, not constrained to be centered at $C = 1.0$. This relatively high correlation level was chosen to allow good fits for points near the edge of the images when the cross-correlation did not quite reach 0.5. Some examples of these fits are shown in Figs. 8(c) and 8(d), which correspond to the 2D correlation maps in Figs. 8(a) and 8(b) for the two shots with the largest field angle misalignments of Figs. 3(b) and 3(c).

The points used for the elliptical fits in Figs. 8(c) and 8(d) are shown as small black dots, and the fits are shown by red ellipses overlaid on these dots (most ellipses overlay the dots so well that they are not easily seen). Superimposed on these ellipse fits are red arrows showing the relative magnitude and direction of the calculated B field misalignment at each point on this 5×3 grid. The magnitude of the largest misalignment arrow for the shot in (a) is $\Theta = 20.3°$ at the grid point (r,p)= (−6 cm, +7.5 cm), which is also the maximum misalignment angle for the entire database, and the largest misalignment arrow for the shot in (b) is $\Theta = 13.3°$ at the grid point (−3 cm, −7.5 cm). Many of the elliptical fits in Fig. 8 appear to be elongated along the B field misalignment direction for these two shots with the largest poloidal misalignments. However, some of the elliptical fits for smaller misalignment magnitudes (arrow lengths) are clearly not elongated in the misalignment direction, e.g., at (+6 cm, −7.5 cm) in Fig. 8(c) and (+3 cm,+7.5 cm) in Fig. 8(d). Note that the ellipse fits at −6 cm for Fig. 8(d) are not shown

since these points were too close to the left edge of the image to get good fits to the cross-correlation functions.

A database was constructed of these correlation tilt angles φ and ellipticities ε, along with the corresponding B field alignment angles for each point in the 5×3 spatial grid for the 20 shots in Table I. Poor elliptical fits were eliminated when one axis of the ellipse was <0.3 cm (less than one pixel), which usually occurred at radii of r = −6 cm due to the correlation function overlapping the left edge of the image or due to excess noise in the data at some points with r = +3 cm and +6 cm, which caused the cross-correlation to fall below 0.8 at one pixel from the origin. Fits were also eliminated for which the axis of the ellipse was off-center by >1 cm from the correlation origin. The resulting database had 237 of the 300 possible spatial array points for these shots. The ellipticity was significant (i.e., $\varepsilon \geq 1.3$) for 93% of these 237 points so that the corresponding tilt angles φ were usually well defined.

The average 2D correlation tilt angle direction in this database was $\varphi = 87° \pm 34°$, which is near to the poloidal (i.e., vertical) direction of $\varphi = 90°$, and the average ellipticity of the correlation functions (major/minor axis lengths) was $\varepsilon \sim 2.2 \pm 0.9$. These results are qualitatively consistent with the 1-D correlation results where $L_{pol}/L_{rad} \sim 1.4$ (see Sec. III C), i.e., with the turbulence elongated in the poloidal direction. There was no correlation between the measured tilt angle direction and the ellipticity for the set of 237 points as a whole (none was expected).

C. Effect of B field misalignment on cross-correlations

Figure 9(a) shows the measured cross-correlation function tilt angle φ vs. the *direction* of the B field misalignment angle Φ in this database, both measured counter-clockwise from the radially outward (horizontal) direction. Note that the calculated direction of the B field misalignment is plotted within 0°–360°, but the correlation tilt angle can only be measured within 0°–180°. All 237 points in the database are shown with red circles, but points with a relatively large misalignment magnitude of $\Theta \geq 10°$ are also highlighted with blue dots (143 points). Many of the blue dots lie near the diagonal lines where these two angles are equivalent, suggesting that the measured cross-correlation direction in these cases is at least partially determined by the misalignment direction. However, some blue points and most red points are far from these diagonals, showing no clear relationship between the measured cross-correlation tilt and the calculated B field misalignment. The largest misalignment points of shots #141741 ($\Theta = 20.3°$) and #138848 ($\Theta = 13.4°$) lie near the diagonal lines, but the more typically misaligned center point of #140392 ($\Theta = 8.6°$) does not lie near these lines.

Figure 9(b) shows the *difference* between the measured correlation tilt angle φ and the calculated B field misalignment direction Φ as a function of the *magnitude* of the misalignment angle Θ. For relatively small misalignment magnitudes of $\Theta \leq 10°$, this difference is large and random, suggesting that the correlation tilt angle is not strongly affected by the B field misalignment, as expected for small
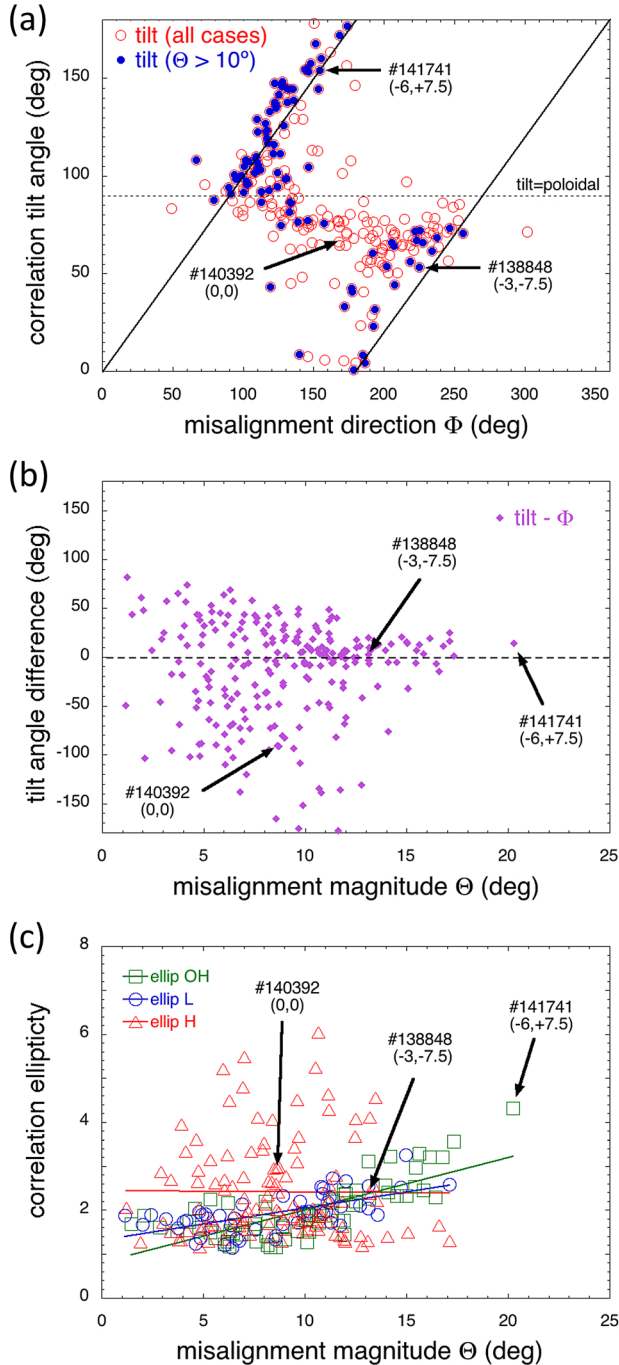
FIG. 9. (a) The measured cross-correlation function tilt angle φ vs. the B field misalignment direction Φ for the 237 points in the database (red circles). Points with large misalignment magnitudes of $\Theta \geq 10°$ are highlighted with blue dots. There is a trend for the points with blue dots to fall along the diagonal line where the tilt angle equals the misalignment angle. (b) The difference between the measured tilt angle and the direction of the B field line angle (φ-Φ) vs. the magnitude of B field misalignment angle Θ. The difference between these angles becomes small for $\Theta \geq 15°$ or so, suggesting that the misalignment affects the correlation tilt angle. (c) Only a slight trend for the ellipticity to increase with the magnitude of the misalignment angle, as shown by the linear fits to the data sorted into Ohmic, L-modes, and H-modes separately. However, there are many cases of relatively high ellipticity with relatively low Θ and *vice versa*.

misalignments. However, for relatively large misalignments of $\Theta \geq 15°$, the difference between these two directions is mainly $|(\varphi\text{-}\Phi)| \leq 20°$, suggesting that the correlation tilt is affected by this large misalignment. A gradually increasing

effect with Θ is not surprising since it should start to occur as the smearing length becomes comparable to the correlation length, as discussed in Sec. III C. Note that all but one of the 15/237 points with $\Theta \geq 15°$ occur at the poloidal location p = 7.5 cm, which is where the misalignment is the largest for this database. Thus, this effect was not significant in the previous analyses done at p = 0 cm and r = −2 cm to 4 cm.[14]

Figure 9(c) shows the corresponding results for the ellipticity of the cross-correlations ε vs. the magnitude of B field misalignment angle Θ. The data for this plot are also partitioned into Ohmic, L-mode, and H-mode shots, according to the designations shown in Table I. The ellipticity tends to be slightly higher in H-mode shots, as discussed further in Sec. IV D. Averaged over all shots, there is a slight increase from $\varepsilon = 2$ to 3 over the entire range of misalignment angles, but there are also many cases with relatively high ellipticity at relatively low Θ and *vice versa*. This suggests that the misalignment effect does not dominate the measured ellipticity of the cross-correlation functions. This is qualitatively consistent with the estimates of the spatial smearing effect of Sec. III C, which showed that misalignment effects on the correlation lengths were small (i.e., <10%), assuming a GPI cloud size from DEGAS 2.

In summary, Figs. 9(a) and 9(b) provide indirect but fairly clear evidence that the tilt of the 2D correlation functions is affected by the local GPI viewing angle when the magnitude of this angle is roughly $\Theta \geq 15°$. Figure 9(c) also shows a slight systematic increase in the ellipticity with this misalignment. Further discussion of these results is in Sec. V B.

D. Parametric variation of correlations

This section describes the variations in the correlation tilt and ellipticity within the database of Sec. IV C, which contained 237 elliptical fits to the local cross-correlation functions evaluated on a 5 × 3 spatial grid for 20 shots. That database was supplemented with global and local edge plasma parameters from the previous GPI database.[14]

Figure 10(a) shows the measured variations of the cross-correlation tilt angle φ vs. the radius (r) with respect to the separatrix. There is little or no systematic variation of the tilt angle with the radius but instead a large scatter centered about $\varphi \sim 90°$, which corresponds to an elongation in the poloidal (i.e., vertical) direction. Note that many of the points at a radius of −6 cm are missing since these were excluded due to poor fits at the edge of the image (see Sec. IV C). Figure 10(b) shows the tilt angle vs. the poloidal coordinate (p) within the image, which *does* seem to show a systematic increase in the correlation tilt angle with the vertical height, with average tilts of $\varphi = 69° \pm 35°$ at p = −7.5 cm and $\varphi = 101° \pm 22°$ at p = +7.5 cm. This variation could be related to the flux surface geometry or shear, as discussed further in Sec. V B.

Fig. 10(c) shows the correlation tilt angle vs. the vertical magnetic field line angle θ_z, as listed in Table I. The lowest field line angle $\theta_z = 26°$ (#141741) corresponds to the alignment map in Fig. 3(b) where the best alignment is near the bottom of the image, and the highest field line angle $\theta_z = 43°$ (#138848) corresponds to the alignment map in Fig. 3(d) where the best alignment is near the top of
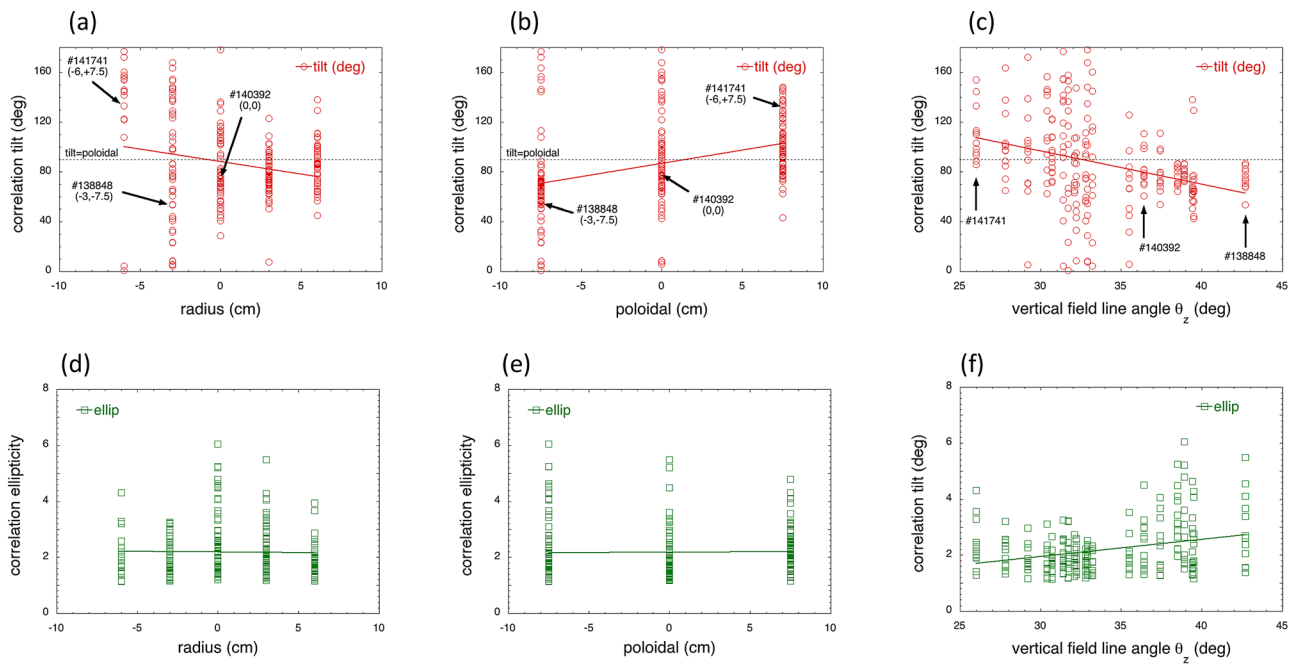
FIG. 10. (a) and (b) The variations of the cross-correlation tilt angle φ with respect to the radius (r) and poloidal height (p) within the image. (c) The correlation tilt angle φ vs. the vertical magnetic field line angle θ_z. The ellipticity variations with these same parameters are shown in parts (d)–(f). There is a trend for the tilt angle to increase with p and to decrease with θ_z but with significant scatter in both cases. All plots show linear fits to the data.

the image (#141984). For these extreme cases, the measured correlation tilt angles are almost all $\varphi > 90°$ and $\varphi < 90°$ (respectively), as also seen in Fig. 8. However, for intermediate cases such as #140392, the scatter in the tilt angle is large compared with any systematic variation with the field line angle, thus suggesting little or no causal relationship between the measured correlation tilt and the B

field geometry near the optimal vertical alignment angle of $\theta_z = 36°$.

The ellipticity does not vary significantly with the radial or poloidal grid point location, as shown in Figs. 10(d) and 10(e). There was a slight increase in the average ellipticity with θ_z, as shown by the linear fit in Fig. 10(f), but the scatter is large compared to the linear trend.
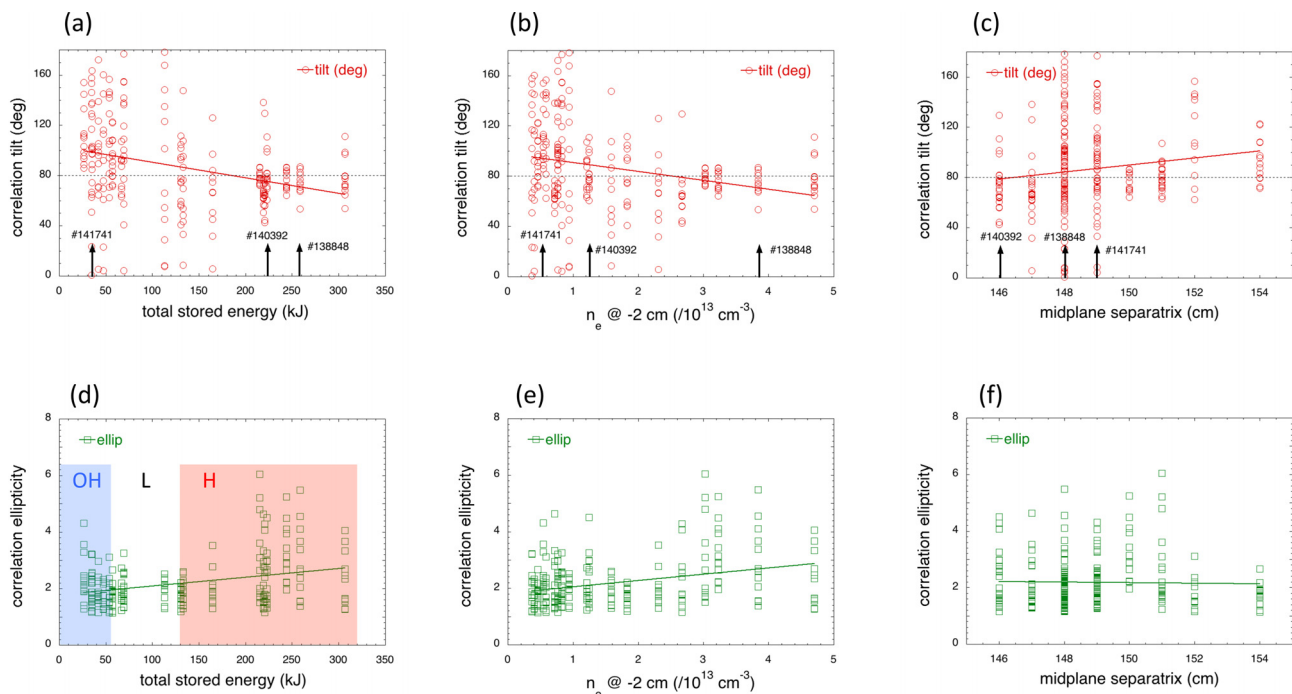

FIG. 11. (a) and (b) The variations of the correlation tilt angle φ with the global stored energy W and the local plasma density at 2 cm inside the separatrix, where both of these parameters are the lowest in Ohmic shots such as #141741 and highest in high-power H-mode shots such as #138848. (c) The tilt angle variations with the midplane separatrix location R_{sep}. (d)–(f) The correlation ellipticity as a function of these same variables. There are trends for the tilt angle to decrease with W and edge density and for the ellipticity to decrease with these same variables although there is considerable scatter in all cases. The data in (d) are sorted into Ohmic, L-mode, and H-mode regimes by the shaded regions. All plots show linear fits to the data.

Figure 11 shows the variations of the measured correlation tilt and ellipticity with some of the plasma parameters. Figure 11(a) shows the tilt angle decreasing with increasing plasma stored energy W, and Fig. 11(b) shows a similar trend with increasing edge plasma density n_e (measured by Thomson scattering 2 cm inside the separatrix), although there was a large scatter over the database as a whole. For example, the tilt angle was $\varphi = 114° \pm 23°$ in the Ohmic shot #141741 with $W = 26$ kJ, and $\varphi = 73° \pm 11°$ for the high-power H-mode shots #138848 with $W = 259$ kJ. Similarly, there was a slight increase in the tilt angle with respect to the midplane separatrix location R_{sep} in Fig. 11(c); for example, the shot with the smallest $R_{sep} = 146$ cm of #140392 has an average tilt angle of $82° \pm 15°$, while the shot with the largest $R_{sep} = 154$ cm (#141984) has a tilt of $95° \pm 17°$. There were only small variations of the ellipticity with these parameters, as shown in Figs. 11(d)–11(f), although the average ellipticity is the lowest for the shots with the largest $R_{sep} = 152$–154 cm.

The shots in the database plots of Figs. 10 and 11 were not explicitly sorted according to the discharge mode (Ohmic and L/H mode), but this is done for illustration in the plot of ellipticity vs. stored energy in Fig. 11(d), using the same data as in Fig. 9(c). The shots with stored energy $W \leq 53.4$ kJ were Ohmic, the shots with $W = 130$–307 kJ were H-mode, and the shots in between were L-mode, as shown by the shaded regions. The average ellipticities were $\varepsilon = 2.0 \pm 0.64$ for Ohmic, $\varepsilon = 1.9 \pm 0.44$ for L-mode, and $\varepsilon = 2.4 \pm 1.1$ for H-mode cases, showing a slightly larger ellipticity for H-modes. However, the spread or scatter in ellipticity (and also tilt angle) within each mode was also large, as also shown in Fig. 9(c).

The database was further examined for systematic variations in the correlation tilt and ellipticity with other plasma parameters such as the edge T_e, plasma κ, q_{95}, dr_{sep} (radial distance between upper and lower separatrices), lithium content, and also the local turbulence correlation lengths and turbulence poloidal velocities. However, there were little or no clear systematic trends in these other database plots (not shown in figures). As in the case of the previous study of turbulence variations,[14] this absence of clear trends may in part be due to the diversity of the shot list, which represented many different experiments and not systematic scans of an individual plasma parameter.

E. Negative cross-correlations

Another general feature of the cross-correlation examples of Figs. 7 and 8 were the negative regions, e.g., in Fig. 7(a) which had $C \sim -0.5$ (dark blue) in many cases. These negative regions are where the turbulence has (on average) the *opposite sign* to that at the correlation origin point. Such negative correlation regions might be caused, for example, by an interchange or wave-like fluctuation pattern which consistently exchanges density between the negative and positive correlation regions. Random turbulence fields should have no significant negative correlation regions.

Correlation maps are shown in Fig. 12 for three additional shots with large negative correlations for the poloidal $p = 0$ cm grid points only (for brevity). In Fig. 12(a), the dark blue regions are radially outside the correlation origin for r $= -6$ cm and r $= -3$ cm and highly elongated in the poloidal direction, while the negative regions for r $= 0$ cm and r $= 3$ cm are radially inside the correlation origin [to some degree, this is just a result of the symmetry of the correlation function with respect to $\mathbf{x}_1$ and $\mathbf{x}_2$ in Eq. (1)]. In Fig. 12(b), the dark blue regions cover a larger area than the red (positive) correlation regions and are again outside the correlation origin for r $= -6$ cm and -3 cm and inside the origin for r $= 3$ and 6 cm. In Fig. 12(c), there are negative correlations both above and below the positive correlation region for r $= -6$ cm, -3, and 0 cm. Negative correlations are almost absent for the r $= 6$ cm regions in (a) and (c). Evidently, there is a wide variety of negative correlation patterns for this database.
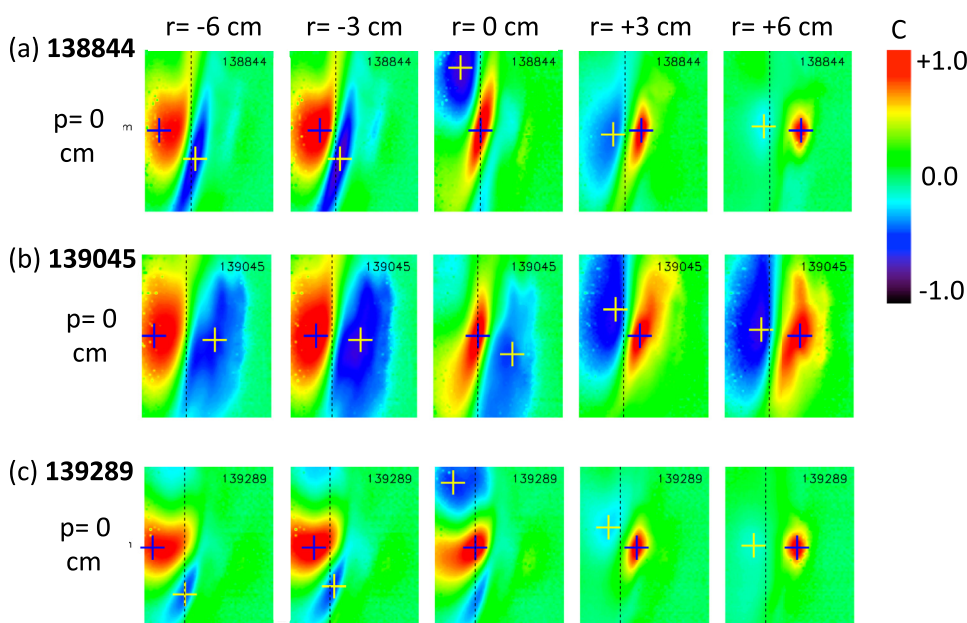

FIG. 12. Maps of the 2D correlation function for three shots with large negative correlations (dark blue regions), starting from radii r $= 0$ cm, ± 3 cm, and ± 6 cm, but only for the middle poloidal location p $= 0$ cm. There is a wide variety of negative correlation patterns within these images for this database.

Note that all the normalized 2D spatial correlation maps are averaged over a 10 ms time period for each shot, as discussed at the beginning of Sec. IV. Thus, the negative regions of the correlation maps are persistent features of the fluctuation structure over this time period. For hypothetical wave-like perturbations of a given wavelength, the location of the negative correlation structure should be independent of the frequency and phase of the wave (for $f > 0.1$ kHz), as discussed further in Sec. V D.

As far as we know, there is no mechanism by which the misalignment of the GPI view with the B field line could cause or significantly affect these negative correlations, since their main effect is to spatially smear the underlying correlation pattern. However, for reference, the perfect alignment points for the three shots in Fig. 12 are at (a) $r = 7.1$ cm, $p = 3.3$ cm, (b) $r = 7.9$ cm, $p = 3.0$ cm, and (c) $r = 10.5$ cm, $p = -3.3$ cm. The misalignments do not appear to significantly affect the positive correlation regions in these cases.

The negative correlations were characterized in two ways: first, by the magnitude and location of the *minimum* value of the negative cross-correlation within the images, "cmin," the locations of which are shown by the yellow "+" in each image in Figs. 7, 8, and 12. The second way was the ratio of the total negative to positive correlation strength "neg/pos" in each image, i.e., the ratio of the separately summed negative and positive correlation coefficients, averaged over all pixels. Note that both are imperfect characterizations since the negative correlation regions often overlap the edge of the images, especially when the origin is at the lowest radii $r = -6$ cm or for the poloidal locations of $p = \pm 7.5$ cm. These two measurements were added to the

correlation database of Sec. IV C for all 15 origin points for all 20 shots. As for the positive correlations, shots with very similar plasma parameters had similar negative correlation patterns.

Some database results of these negative correlations are shown in Fig. 13, with both the minimum values "cmin" and the negative/positive ratios "neg/pos" shown in each plot. The average minimum correlation coefficient over the whole database is cmin $= -0.30 \pm 0.15$, and the average neg/pos $= 0.25 \pm 0.24$. Overall, the negative correlations are smaller than the positive correlations, and these two measures of negative correlation had a roughly linear relationship with each other (not shown).

There was a small systematic variation of these negative correlations with the origin radius, as shown in Fig. 13(a), with somewhat lower-level negative correlation at the largest radius, also illustrated in Fig. 12. However, in Fig. 13(b), there was no variation of the negative correlations with the poloidal location of the origin, as there was for the positive correlations in Fig. 10(b). There was some increase in the negative correlation with the vertical field line angle in Fig. 13(c) and also with the total stored energy in Fig. 13(d) and edge density in Fig. 13(e), but the scatter in all cases is large. There was no overall trend with the midplane separatrix location R_{sep} in Fig. 13(f), but there were unusually low negative correlations for the largest midplane separatrix positions of $R_{sep} = 152$ and 154 cm. There are no clear trends of these negative correlations with the other plasma parameters mentioned in Sec. IV D, or with the turbulence poloidal or radial correlation lengths, or with the (positive) correlation tilt angles or ellipticities.
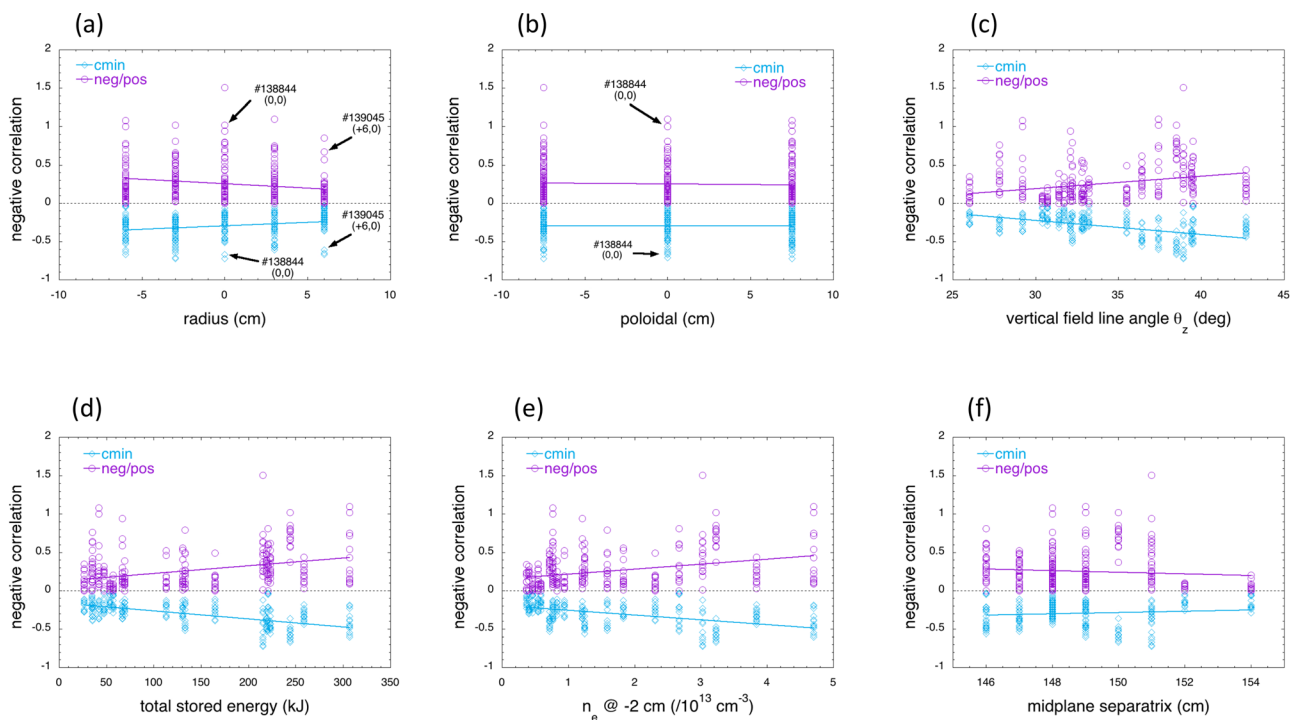

FIG. 13. (a) and (b) The variations of the minimum negative values "cmin" and the negative/positive ratios "neg/pos" vs. radial and poloidal grid location in this database. (c) The variations vs. the vertical field line angle θ_z. (d)–(f) The same negative data vs. the stored energy W, the edge density, and the midplane separatrix radius R_{sep}. There is a trend for decreasing negative correlation for the increasing radius but increasing negative correlations for increasing W, θ_z, and edge density. All plots show linear fits to the data.

The spatial locations of the minimum negative correlation coefficients "cmin" are shown in Fig. 14. The radial distance "δr" between this minimum location in radius and the correlation origin radius is shown as a function of the origin radius in Figure 14(a). This shows a trend for δr to be positive for negative r (i.e., origin points inside the separatrix) and negative for positive r, as seen in the images in Figs. 12(a) and 12(b). Figure 14(b) shows a similar but less pronounced trend for δp vs. p. At least some of this trend is due to the effect of the image boundaries, particularly at the low r edge, as shown in the 2D plot of the location of "cmin" within the (64,80) pixel grid in Fig. 14(c). The origin points (shown by red circles) near the left edge of the image in Fig. 14(c) may have negative regions beyond the left edge, which are not included in Fig. 14(a). The relative locations δr and δp of "cmin" with respect to the origin points are shown in Fig. 14(d). Despite the limitation of the image size, there is a clear trend for the minimum negative correlations to cluster $\sim$5–10 cm inside and above and $\sim$5–10 cm outside and below the correlation origin, particularly for large negative correlations (cmin < -0.3) shown as dark blue dots in this figure. This is an unexpected and unexplained result.

In summary, there are significant regions of negative cross-correlation in this database, with an average of cmin $= -0.30 \pm 0.15$ and neg/pos $= 0.25 \pm 0.24$, with some relatively weak trends with plasma parameters, and with an interesting spatial clustering of the minimum correlation points shown in Fig. 14(d). Possible causes of these negative correlation results will be discussed in Secs. V D–V F.
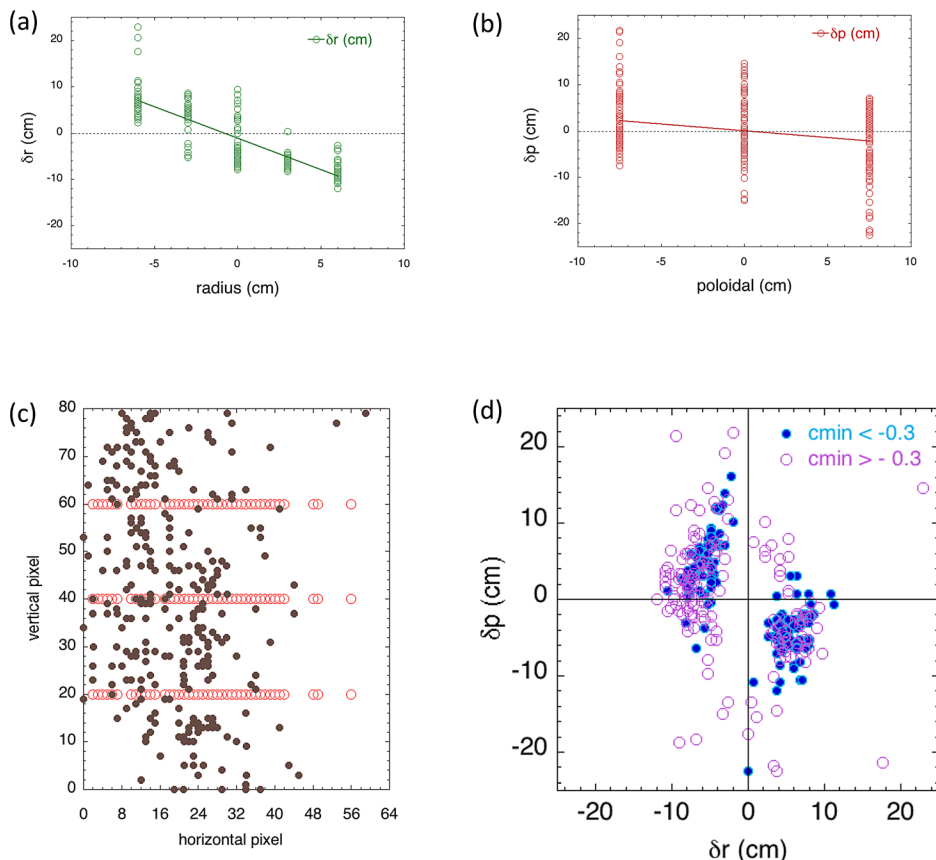
F. Correlation function shapes

Typical 2D correlation functions were already plotted in Figs. 7, 8, and 12, but in that format, it was difficult to see the 1-D shapes of the correlation functions. Here, for the sake of clarity, we show examples of the 1-D radial and poloidal cross-correlation functions for the p $= 0$ poloidal grid points only (for brevity).

Figures 15(a) and 15(b) show the radial and poloidal cross-correlation functions for shot #141984 for the usual five radii r $= 0$ cm, ± 3 cm, and ± 6 cm with respect to the separatrix, all for p $= 0$ cm. This was the shot with the large separatrix radius, as previously shown in Fig. 7(b), so the origin points at C $= +1.0$ are distributed toward large radii in the radial profiles of Fig. 15(a). The radial correlation functions in (a) are clearly non-Gaussian in most cases, with an extended tail toward low radii for the r $= -3$ cm and -6 cm points. The poloidal correlation functions in (b) are nearly Gaussian, with little or no negative correlations in this shot. The correlation functions at r $= +6$ cm (red) fell below 0.8 at one pixel poloidally from the origin, which eliminated its elliptical fit from the database.

Figures 15(c) and 15(d) show the same profiles for shot #139045, which had the large negative cross-correlation regions, as shown in Fig. 12(b). The radial correlation functions in (c) are clearly non-Gaussian with a near-dipole shape, but the poloidal correlation functions in (d) are again close to Gaussian. The radial correlation function for r $= -6$ cm overlapped the left edge significantly, and its elliptical fit was eliminated from the database since it was not centered with 1 cm of the origin.

FIG. 14. The locations of the minimum negative correlations in this database. The radial and poloidal distances "δr" and "δp" between the correlation minimum and the correlation origin are shown in (a) and (b) as a function of the radial and poloidal grid locations. The 2D location of these minima in the (64,80) pixel grid is shown in (c) along with the correlation origins as red circles. (d) The distances "δr" vs. "δp" for cmin < -0.3 and cmin > -0.3. There is a fairly clear trend for the minimum correlations to cluster $\sim$5–10 cm inside and above and $\sim$5–10 cm outside and below the correlation origin, particularly for larger negative correlations (cmin < -0.3).
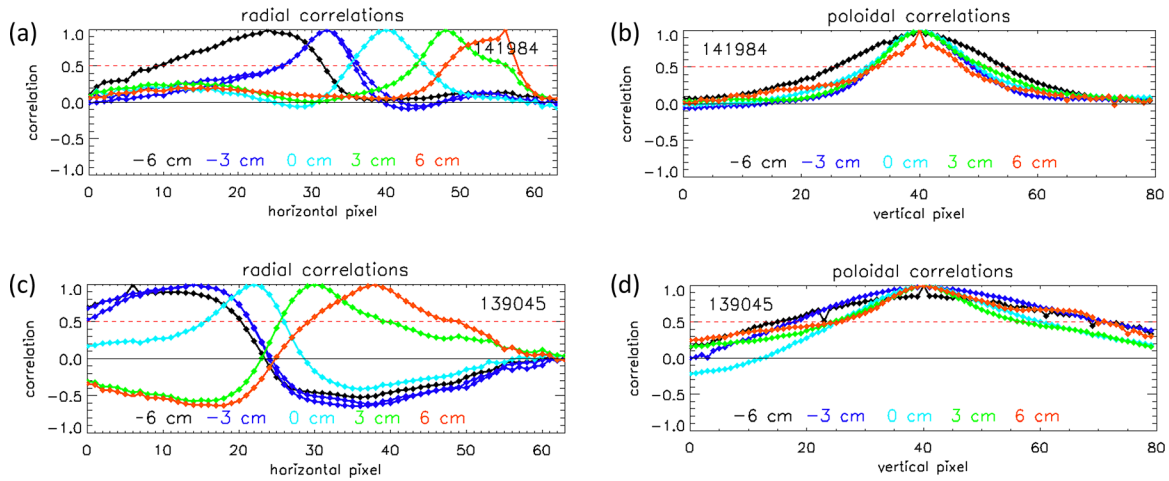
FIG. 15. (a) and (b) The radial (i.e., horizontal) and poloidal (i.e., vertical) cross-correlation functions for shot #141984 for origin radii r = −6 cm, −3 cm, 0 cm, +3 cm, and +6 cm and for p = 0 cm. The color code for origin radii is shown at the bottom of the figure. The radial correlation functions are mainly non-Gaussian, and the poloidal correlation functions are near Gaussian. In parts (c) and (d) are the same profiles for shot #139045, which is the shot with the large negative cross-correlation regions in Fig. 12(b). The radial correlation functions have a nearly dipole shape, and the poloidal correlation functions are again close to Gaussian.

In general, most of the correlation functions for the 5×3 spatial grid for these 20 shots have shapes in between the four cases shown in Fig. 15. One exception was shot #139289, which has negative correlation regions both above and below the origin, as shown in Fig. 12(c), as discussed further in Sec. V E.

V. DISCUSSION

This section discusses some theoretical interpretations of the experimental results described in Sec. IV. A summary of the experimental results and the conclusions are in Sec. VI.

A. Effects of GPI misalignment

The geometrical smearing effects on the 2D cross-correlation measurements due to GPI viewing misalignment are discussed in Sec. III. The calculated misalignment between the GPI view and the local magnetic field direction varies within the image and from shot-to-shot, as shown in Fig. 3, but was relatively small over the regions of interest, averaging $\Theta \sim 9°$. Comparison of the measured 2D correlation tilt angles with the calculated misalignment angles in Fig. 9(b) suggested that the tilt angle was affected by misalignments when $\Theta > 15°$ ($\sim 6\%$ of the database), which corresponds to a smearing length of $\delta \sim L_{II} \tan \Theta \sim 3.2$ cm. This smearing effect is somewhat lower than the turbulence correlation lengths of $\sim 5-6$ cm, perhaps suggesting that the DEGAS 2 estimate of L_{II} is too small. More accurate corrections for such large misalignment effects can only be done once the GPI gas cloud size and shape are measured, e.g., using a camera viewing perpendicular the B field line.

One important consequence of this misalignment effect is that small-scale structures of ≤ 1 cm scale cannot be resolved with GPI in NSTX unless the misalignment angle is kept below $\Theta \sim 3°$ or alternatively if the parallel length of the GPI gas cloud is reduced, e.g., with a supersonic gas nozzle.[31] This resolution limit might improve with helium GPI, compared to the deuterium GPI used in this paper, since the dissociation energy of the deuterium molecules tends to increase the GPI cloud size.

B. Effects of magnetic shear

It is well known that magnetic shear changes the 2D shape of tokamak magnetic flux tubes along the poloidal direction and that the edge turbulence structure tends to follow the shape of flux tubes. Experimental evidence for this effect has been obtained by comparing the turbulence cross-correlation tilting at two different poloidal locations, e.g., in Tore-Supra and EAST[33] and Alcator C-Mod.[11] In the present experiment, a systematic change in the correlation tilt angle with the poloidal location is shown in Fig. 10(b), with tilts of $\varphi = 69° \pm 35°$ at p $= −7.5$ cm and $\varphi = 101° \pm 22°$ at p $= +7.5$ cm (but with no significant change in ellipticity over this range). The effect of magnetic shear is investigated in this section.

The effects of magnetic shear on the 2D shape of the cross-correlation function were evaluated using field line mapping of flux tubes based on EFIT02 magnetic equilibrium reconstructions. Initial flux tubes were assumed at p = 0 cm at radii of r = 0 cm, ±3 cm, and ±6 cm from the separatrix. All assumed flux tubes had an initial ellipticity $\varepsilon = 2.2$, a tilt angle $\varphi = 90°$, and a radial width of 2 cm, as shown in Fig. 16(a) by the black dashed ellipses in the (R,z) plane for shot #138848. These initial flux tubes were projected to other poloidal locations via a toroidal translation with respect to the GPI image plane, and the projected flux tube shapes at other poloidal locations are shown at each radius, along the flux surface contours. The mapping of these flux tubes into the GPI image plane is shown in Fig. 16(b). The curvature of the flux surface and the magnetic shear have an opposite effect on the flux tube tilt as evaluated in the GPI image plane. Flux surface curvature leads to an increasing tilt angle (i.e., more counter-clockwise) with the increasing poloidal location, while magnetic shear results in
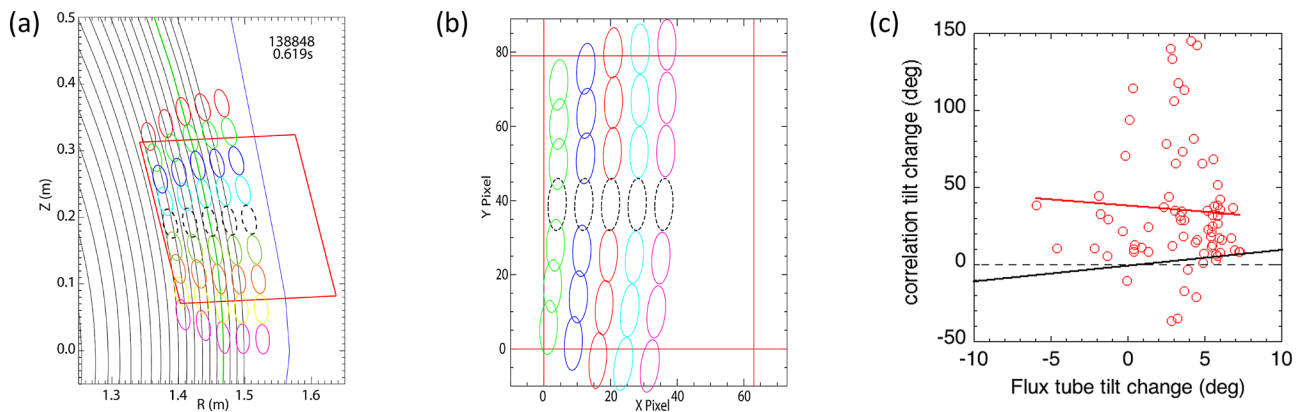
FIG. 16. (a) The effect of magnetic shear on flux tubes in the (R,z) plane, starting with ellipses at $p = 0$ cm and $r = 0$ cm, ± 3 cm, and ± 6 cm (black dashed lines), assuming $\varepsilon = 2.2$, $\varphi = 90°$, and a radial width of 2 cm. The projected flux tube shapes at other poloidal locations are also shown for each radius, along with the variations in the tilt angle of the flux surfaces in this region (the green flux line is the separatrix and the blue line is the RF limiter shadow). The mapping of these flux tubes into the GPI image plane is in (b), showing a trend for the increasing tilt angle (i.e., more counter-clockwise) with the increasing poloidal pixel location. (c) Database results for the measured correlation tilt change over $p = \pm 7.5$ cm vs. the tilt change calculated from the model in (b) over $p = \pm 7.5$ cm for all radii and shots. The measured tilt changes (fit by the red line) are significantly larger than expected from this magnetic shear model (black line).

a decrease in the tilt angle with the increasing poloidal location. Changes in ellipticity over this range of poloidal angle are small.

Figure 16(c) shows the measured change in the correlation tilt angle over $p = \pm 7.5$ cm, previously shown in Fig. 11(b), vs. the calculated flux tube tilt changes as analyzed in Fig. 16(a) for all shots in the database. The calculated flux tube tilt angle changes by $-6°$ to $+7°$ over this poloidal range, including both the magnetic shearing and flux surface tilt effects, whereas the measured correlation tilt angle changes over the much larger range of $-36°$ to $+145°$. Thus, only a small fraction of the variation in the observed correlation tilt angle within the poloidal range of the GPI image can be explained by the combined effects of magnetic shear and flux surface curvature, at least within this simplified model. The cause of the large measured change in the correlation tilt angle over the poloidal range of the image is presently not understood.

C. Effects of flow shear

There is some experimental evidence that rapidly sheared plasma flow can affect edge turbulence in tokamaks[5,9,16] and linear devices.[18,19] Qualitatively, we might expect that with large poloidal flow shear, the radial correlation length should decrease and the poloidal correlation length should increase, so both the ellipticity and tilt of the correlation function should be affected. A dimensionless form of the local flow shear of $S = (dV_{pol}/dr)(L_{rad}/L_{pol})\tau_{auto}$ was previously calculated for GPI data in NSTX,[34] where V_{pol} is the poloidal speed of the turbulence (not the fluid speed) and τ_{auto} is the turbulence autocorrelation time. A significant change in the correlation function can be expected when $|S| > 1$.

A preliminary evaluation of this shearing effect for the 20 shots in the present database is shown in Fig. 17. Figure 17(a) shows the radial profile of the time-averaged V_{pol} of the turbulence previously derived from time-delayed cross-correlation analysis,[14] with positive velocities upward in the

GPI field of view (i.e., in the electron diamagnetic drift direction). There is large spread in V_{pol} since this database includes Ohmic, L-mode, and H-mode shots, but all velocities lie within the range $|V_{pol}| \leq 5$ km/s. Note that the spatial blurring of the turbulence structure due to the poloidal motion of the turbulence over one ~ 2.1 μs frame integration time is ≤ 1 cm. The radial profile of τ_{auto} is shown in Fig. 17(b) and is in the range τ_{auto}(FWHM) of ~ 20–40 μs.

In Figs. 17(c) and 17(d), the ellipticity and tilt of the cross-correlation functions are shown as a function of dV_{pol}/dr for each shot, calculated from $[V_{pol}(-2$ cm$)-V_{pol}(+2$ cm$)]$ for the $(r,p) = (0,0)$ points and $[V_{pol}(+2$ cm$)-V_{pol}(+4$ cm$)]$ for the $(3,0)$ cm points. The same data are plotted vs. the normalized shear S in Figs. 17(e) and 17(f). There seems to be a trend for the ellipticity to decrease with increasing dV_{pol}/dr and S and for the tilt angle to increase with increasing dV_{pol}/dr but with little or no consistent change in ε or φ with the absolute values of dV_{pol}/dr or S. However, there is considerable scatter in this analysis, as also observed in a previous study of flow shear effects on blobs.[35] Thus, a more detailed study with systematic parameter scans and detailed error analysis is warranted, including the analysis of the *fluctuations* in the shape of the correlation functions and the corresponding shear flows, which is beyond the scope of the present paper.

D. Negative correlation from waves

A random space-time signal with a typical spatial scale of $\sim L$ will tend to produce a Gaussian-shaped cross-correlation function with a spatial width $\sim L$ but with only small randomly generated negative correlation regions. At the other extreme, perturbations with a pure sinusoidal wave-like form should have a sinusoidal spatial cross-correlation function, with a negative amplitude of cmin $= -1$ at half the spatial wavelength. Note that the normalized spatial cross-correlation maps calculated using Eq. (1) are averaged over 10 ms (e.g., Fig. 12), so a propagating sine wave would be seen as a spatial sine wave in the correlation map since the
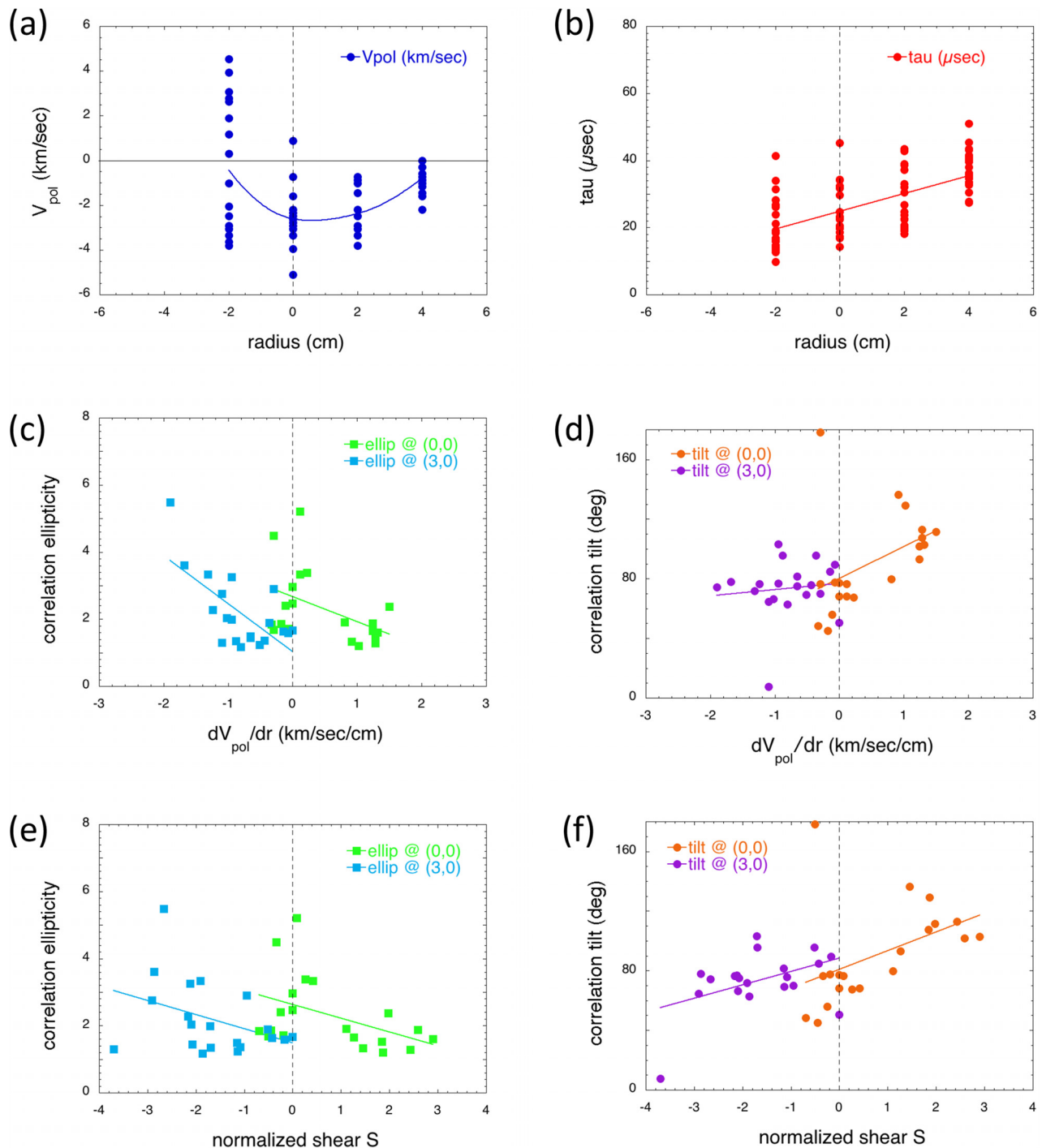
FIG. 17. Flow shear effects on correlations, with (a) and (b) showing the turbulence poloidal velocity V_{pol} and autocorrelation times τ_{auto} vs. radius for the present shot list, taken from a previous database.[14] (c) and (d) The ellipticity and tilt of the cross-correlation functions at grid points (0,0) and (3,0) vs. the time-averaged local gradient of the poloidal flow of the turbulence, dV_{pol}/dr. (e) and (f) The same data vs. the dimensionless turbulence flow shear $S = (dV_{pol}/dr)(L_{rad}/L_{pol})\tau_{auto}$.

cross-correlation amplitude depends mainly on the *relative sign* of the fluctuations between the origin point and the rest of the 2D map.

Most of the 2D correlation patterns described in this paper had a near-Gaussian poloidal correlation function, as shown in Figs. 15(b) and 15(d). However, previous edge turbulence measurements with both GPI and BES in NSTX have shown partially wave-like poloidal cross-correlation functions in ELM-free H-mode plasmas at the inner edge of

the GPI imaging region, with a negative cross-correlation coefficient of cmin of ~ -0.5 and a poloidal wavelength of ~ 40 cm.[7,8] One example of the correlation function with a similar wave-like spatial period is shown in Fig. 12(c), in which two negative peaks with cmin ~ -0.5 were visible above and below the positive peak at r = 0 cm, with a poloidal wavelength of ~ 25 cm (this was an ELM-free H-mode plasma similar to those mentioned above). There were also some radial wave-like structures with negative peaks both

inside and outside the correlation origin, as shown in Fig. 15(c), but both negative peaks were not visible within the same correlation image, perhaps due to the limited radial size of the image.

These wave-like cross-correlation patterns were not due to normal low frequency MHD activity since shots with such activity were excluded from this database. A separate look at shots which did have large low frequency MHD activity showed cross-correlation functions with a high positive correlation over the whole poloidal range of the GPI image since the wavelength of these perturbations was much larger than 30 cm. An exception occurred during ELM precursors, which were seen as periodic within the GPI poloidal range of the GPI image.[36]

The $\lambda_{pol} = 25$ cm poloidal periodicity observed in the cross-correlation map of Fig. 12(c) and a few other (out of 300) cases has a normalized poloidal wavenumber k_{pol} $\rho_s \sim 0.1$. This is roughly consistent with drift waves or drift resistive modes previously discussed for NSTX[7,24] and with drift-Alfven waves seen in the linear device LAPD.[18] Thus, some of the negative correlation structure in this database can be attributed to drift-like waves, particularly in H-mode cases like Fig. 12(c); however, for most of the present database, there is no clear evidence for poloidal periodicity in the 2D correlation maps, as illustrated in Figs. 15(b) and 15(d). Clearly, further study of partially wave-like correlation functions is warranted, particularly motivated by comparisons to theory.[24–28]

E. Negative correlations from blob-hole pairs

As noted previously in Sec. IV E, there was a small systematic decrease in the negative correlation amplitudes from inside to outside the separatrix, as illustrated in Figs. 12 and 13(a). The radial location of the most negative correlation also varies systematically from inside to outside the correlation origin with the increasing radius, as shown in Fig. 14(a). This section examines whether these results can be attributed to the mechanism of blob-hole pair formation in the edge.

Any process that forms positive-density 'blobs' in the tokamak edge should also create negative-density 'holes' nearby, assuming that the density is conserved in this process. Since there are often high amplitude positive blobs in the NSTX GPI data,[15] these might cause some of the negative correlation patterns in the data.

To test this idea, a simple one-dimensional statistical model describing the correlation of blob-hole pairs was developed. In this model, the space (x) and time (t) dependences of blobs and holes are described by pulses of the form

$$S(x, t; x_0, t_0, v, \delta) = \begin{cases} 0, & t < t_0 \\ e^{-(x-x_0-v(t-t_0))^2/(2\delta^2)}, & t > t_0 \end{cases} \quad (2)$$

where x_0 and t_0 are the birth location and creation time of the blob or hole, v is its velocity, and δ is its spatial size. The normalized density perturbation from the blob-hole pair is then given as

$$\tilde{n}(x, t) = S(x, t; x_0, t_0, v_b, \delta_b) - e^{-(t-t_0)/\tau_h} S(x, t; x_0, t_0, v_h, \delta_h) \quad (3)$$

where we assume $\delta_b = \delta_h$, $v_b > 0$, and $v_h < 0$. The first term represents the blob and the second term the hole. Note that the blob-hole pair grows continuously from zero starting at $t = t_0$ and that the hole decays on a time scale τ_h as it slowly propagates to the left. At longer times, the blob still remains and freely propagates to the right (i.e., to large x). For illustration, we choose the following parameters: $\delta_b = 1$, $x_0 = -1$, $v_b = 1$, $v_h = -0.2$, and $\tau_h = 2$. This choice effectively normalizes the space scale to the blob size and the time scale to δ_b/v_b which is on the order of the auto-correlation time of the blob signal at a fixed spatial point.

We assume that the creation times of individual blob-hole pairs are governed by Poisson statistics, i.e., the waiting times between two different creation events are exponentially distributed.[37] Thus, the probability of exactly K events occurring in a time T is $P_K(\mu) = \mu^K \exp(-\mu)/K!$, where $\mu = T/\tau_w$ and τ_w is the mean waiting time. Numerical results were obtained for $\mu = 0.1$, which describes an intermittent signal, although it can be shown that the correlation defined by Eq. (1) is actually independent of μ in the present model. With the reference point fixed at $x = x_{ref}$, we can examine how the correlation function depends on the observation point x, i.e., we examine $C(x_{ref}, x)$ using $\tilde{n}$ as the signal. Both numerical simulations and analytical calculations were carried out, the latter using methods similar to those in Ref. 38. The numerical and analytical results are in excellent agreement.

The 1-D correlation functions for two different values of x_{ref} are shown in Fig. 18(a). In this figure, the zero of the x-axis has been chosen to be one blob radius to the right of the blob-hole birth zone, i.e., it is expected to be qualitatively similar to the separatrix in experimental data. When the reference point is in the "closed surface" region $x < 0$, the negative correlation appears at $x > 0$ in the "SOL." In this case, the reference point is near the hole and the negative correlation is the blob, as shown by the blue curve in Fig. 18(a). Conversely, when the reference point is in the "SOL" region $x > 0$, it can only detect the blob and the negative correlation appears at $x < 0$ where the hole is located, as shown by the green curve in Fig. 18(a).

The radial dipole pattern seen in these results is similar to that shown in the experimental radial correlations of Fig. 15(c). The position of the negative correlation region relative to the positive one is also qualitatively similar to the trend in Fig. 14(a). More generally, a 1D cut of the experimentally measured 2D correlation functions taken along a line passing through the maximum positive and minimum negative correlation is qualitatively similar to Fig. 18(a), which suggests that this cut-line may be related to the trajectory direction of the blob. The minimum negative correlations in the present model approach -1, which is stronger than that observed experimentally. However, it can be shown that the superposition of white-noise Gaussian turbulence with spatial correlation length $\sigma < \delta$, on top of the blob-hole signal, reduces the magnitude of the negative correlation in the present model. Thus, we conclude that a relatively simple blob-hole model
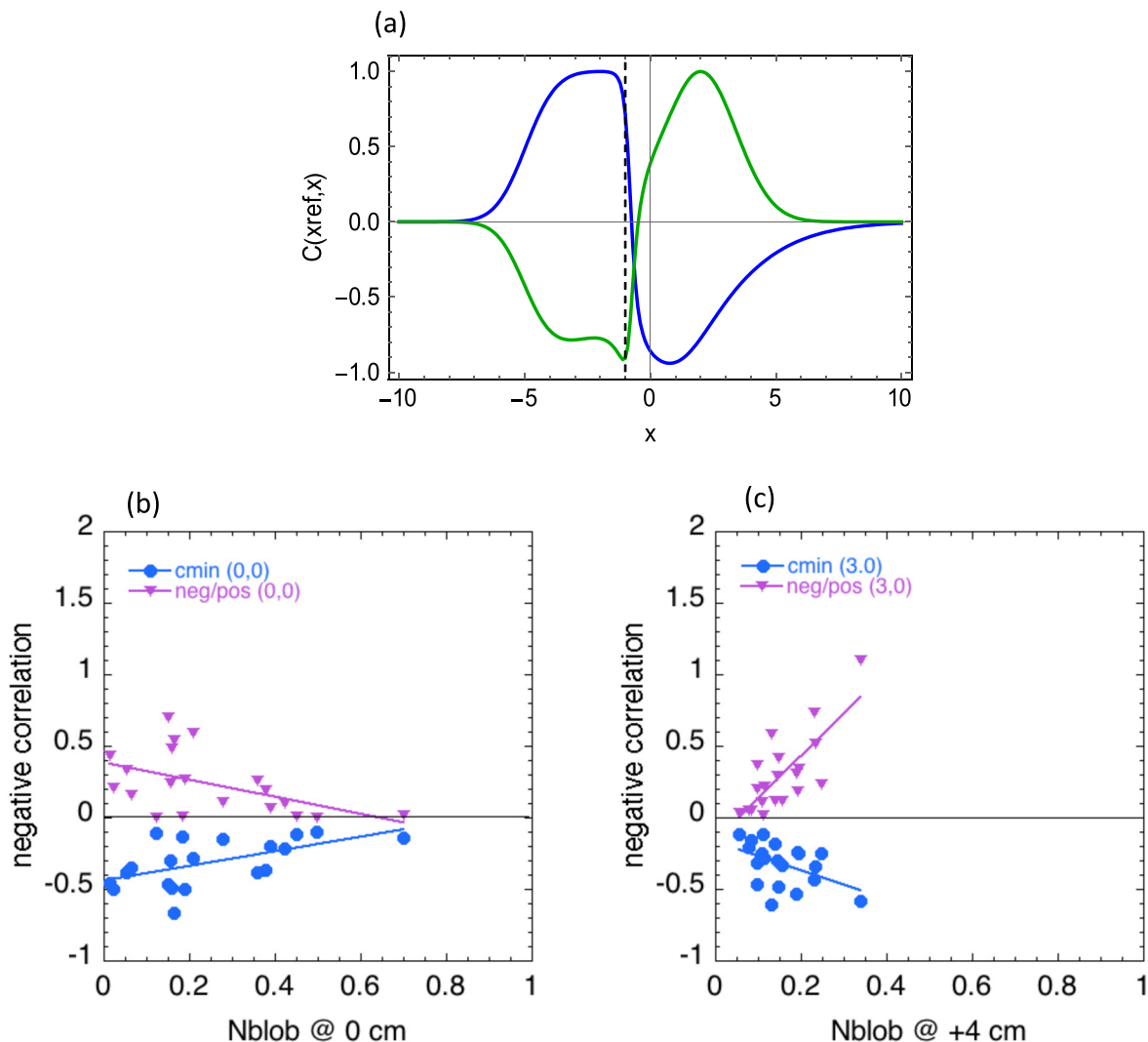
FIG. 18. (a) Radial correlation functions from a 1-D blob-hole statistical model, with $x_{ref} = -2$ (blue) and $x_{ref} = +2$ (green), where x is measured in units of the blob radius δ_b, and where the dashed line at $x = x_0 = -1$ is the assumed blob birth location. (b) and (c) The negative correlation results for grid positions (0,0) and (3,0) vs. N_{blob}, the number of blobs detected per frame within ± 1 cm of r = 0 cm and r = 4 cm, respectively. At r = 0 cm, there was a decrease in negative correlation with increased N_{blob}, while at r = 3 cm, the negative correlations increased with N_{blob}.

can qualitatively describe some of the features of the negative correlations observed in the experimental data.

Figures 18(b) and 18(c) show the negative correlation results for grid positions (r,p) = (0,0) and (3,0) vs. N_{blob}, the number of blobs detected per frame in the present shot list within ± 1 cm of r = 0 cm and r = 4 cm, respectively.[15] The results were mixed: at r = 0 cm, there was a decrease in negative correlation with increased N_{blob}, while at r = 3 cm, the negative correlation increased with N_{blob} at 4 cm. Since there is some randomness to the trajectory of individual blobs, it is possible that blob-hole correlations are only detectable near r = 0 cm when the number of blobs is not too large, which would agree with the observed trend. Conversely, in the far SOL, individual isolated blobs (i.e., propagating positive pulses) produce no negative correlations, as seen for small N_{blob} at 4 cm. It is not clear what to expect when many blobs are simultaneously present and interact in the far SOL. A more detailed analysis of negative cross-correlation regions of blobs should probably be done using a conditional sampling analysis of individual blobs, which is beyond the scope of this paper.

F. Effect of neutral shadowing

Neutral shadowing in GPI is a process by which some of the structure of the plasma turbulence could be transferred onto the otherwise smooth neutral density.[30,39–41] This could in principle cause negative regions in the 2D correlation function, e.g., due to the systematic reduction in local neutral density just inside a large positive blob.

For shadowing to be significant, the turbulent structures need to be comparable to or larger than a neutral mean free path. For a 3 eV deuterium atom, e.g., resulting from dissociation of a deuterium molecule, the mean free path in typical NSTX plasma conditions ranges from about 3 cm near the GPI emission peak ($n_e = 2 \times 10^{13}$ cm^{-3} and $T_e = 60$ eV) to 100 cm or more in the far scrape-off layer ($n_e = 10^{12}$ cm^{-3} and $T_e = 30$ eV). With blob radial correlation lengths in the 2–4 cm range,[15] shadowing may be having an effect near the emission peak and farther in radially. Note that the effects will be much stronger for deuterium molecules or helium atoms than for deuterium atoms since they will have much lower thermal energies and correspondingly shorter mean free paths.

Another factor that limits the amount of shadowing present in these experiments is the reduced directionality of the deuterium atom flux, just as the shadows produced by a diffuse light source are less pronounced than those from a spotlight. First, the actual source of deuterium atoms is not the gas manifold but the volume in which the molecules are dissociated. DEGAS 2 modeling of GPI experiments[32] indicates that this region is a few centimeters from the manifold and, thus, occupies a much larger volume due to expansion of the gas in transit.

Second, the manifold is not the sole source of molecules. Half of the atoms produced by dissociation and charge exchange have radial velocities directed towards the vacuum vessel wall and mean free paths long enough to reach it without undergoing additional collisions. A significant fraction of the atoms will be recycled there as thermal molecules; the net result is an increase in the volume over which the molecules and, thus, their dissociation are spread. The remaining deuterium atoms striking the vessel wall are backscattered. The flux of these atoms is effectively spread in the lateral directions by the trip to the wall and back. Because dissociation and charge exchange are irrelevant for helium, a helium puff will have better directionality and is, thus, more susceptible to shadowing. Note that helium atoms do undergo elastic scattering with deuterium ions, but the momentum exchanged in the process is much less than that provided by resonant charge exchange.

In summary, definitive results on the effect of neutral shadowing in these experiments have not yet been made, either from direct interpretation of the data or from numerical modeling. What is clear from the data is that there is no consistent negative correlation pattern in this database despite the fact that all shots were taken using a GPI gas puff with the same magnitude and time-dependence.[14] More definitive statements regarding shadowing effects in these experiments await 3-D DEGAS 2 synthetic GPI simulations of 3-D turbulent plasma data, such as that produced by the XGC1 code.[28] This work will be reported in a future publication.

VI. SUMMARY AND CONCLUSIONS

Section VI A contains a summary of the experimental results, and Secs. VI B and VI C summarize the conclusions and possible research directions.

A. Summary of experimental results

The shots in Table I used for the present paper were chosen to cover the range of magnetic fields and applied heating power in NSTX, including Ohmic, L-mode, and H-mode regimes. This list excluded shots with large MHD activity or L-H transitions during the analysis time of 10 ms near the peak of the GPI gas puff.

The 2D turbulence cross-correlation functions were evaluated on a 5×3 spatial grid within the GPI images, as described in Sec. IV. In general, the results were quite variable in terms of the ellipticity and tilt of the positive correlation regions, as shown by the red regions in Figs. 7 and 8, and in the magnitude and location of the negative correlation regions, as shown by the blue regions in these same figures. For large misalignment angles ($\Theta > 15°$), the tilt angle of the measured correlation functions is near the misalignment direction Φ, as shown in Figs. 9(b), suggesting that the misalignment affects the tilt angle. On the other hand, the ellipticity of the positive correlation regions did not vary greatly with the magnitude of the misalignment, as shown in Fig. 9(c).

A database study of the parametric variations of the positive correlation tilt and ellipticity is discussed in Sec. IV D, and sample results are shown in Figs. 10 and 11. There were relatively weak variations of the tilt or ellipticity with plasma or geometric parameters, when compared to the scatter in the data. Variations in the negative correlation regions are described in Sec. IV E, and sample results are shown in Figs. 12 and 13. There was a wide variety of negative correlation patterns but with only relatively weak relationships with the geometric, magnetic, or plasma parameters within this database. There were slight trends for the positive ellipticity and negative correlation levels to increase from the Ohmic/L-mode to the H-mode, as shown in Figs. 11(d) and 13(d). One interesting result was a clustering in the location of the minimum negative correlations, as shown in Fig. 14(d).

Examples of the 1-D radial and poloidal shapes of the correlation functions are shown in Fig. 15. Many of the radial correlation shapes were non-Gaussian, and those with large negative correlations had an almost dipole-like radial structure, as shown in Fig. 15(c). The poloidal correlation shapes are mostly Gaussian-like and symmetrical, at least within the GPI image.

B. Conclusions

There was a wide variation in the 2D turbulence correlation patterns described in Sec. IV of this paper, only part of which could be explained using the models discussed in Sec. V. Some specific conclusions are as follows:

(1) The 2D cross-correlation functions were aligned mainly in the poloidal direction with a poloidal correlation length about twice the radial correlation length, corresponding to a correlation tilt angle $\varphi = 87° \pm 34°$ and a correlation ellipticity $\varepsilon = 2.2 \pm 0.9$.
(2) The correlation tilt angles were affected by the misalignment of the GPI viewing angle with respect to the local magnetic field when this angle was $\Theta \geq 15°$, which occurred in ~6% of the points analyzed in this dataset.
(3) The magnetic shear was not large enough to explain the large variations in the tilt angle over the poloidal extent of these GPI images, and there was no clear connection between the measured flow shear and the shape of the measured correlation functions.
(4) There were often significant levels of negative correlation with minimum values cmin $= -0.3 \pm 0.15$, some of which could be qualitatively interpreted as wave-like or blob-hole correlations, but there was no direct evidence for a neutral density shadowing effect.
(5) There were some weak trends in the 2D correlation patterns as a function of plasma parameters, such as an increase in the ellipticity and negative correlation magnitude with increasing stored energy, which are not yet understood.

C. Directions for further research

Future measurements of 2D correlation functions with GPI should be supplemented by a direct measurement of the parallel extent of the gas cloud to better quantify the viewing misalignment effect discussed in Sec. III. The spatial resolution of these measurements could be improved by reducing this parallel cloud length or by having remote control of the GPI viewing direction to better align the optics with a specific local B field. A larger range of poloidal coverage would also help to identify the large-scale wave-like structure seen in some cases, perhaps using a second GPI view.

Dedicated plasma parameter scans should be done to help identify the cause of the measured variations in the turbulence correlation patterns, for example, by varying the edge plasma parameters at a fixed edge B field angle. A more detailed analysis of the relationship between local poloidal flow shear and turbulence structure, which was inconclusive in the present dataset, and between the turbulence structure and its motion in general should be done. The relationship of blobs to holes should be analyzed in detail using blob tracking methods to help quantify the possible connection to negative correlation regions.

The measured turbulence correlation patterns should be directly compared with edge turbulence simulations using a synthetic GPI diagnostic so that the cause of these patterns can be better understood. These simulations should also be used to evaluate the neutral shadowing effect and help evaluate its influence on GPI data.

ACKNOWLEDGMENTS

[1]S. J. Zweben, J. A. Boedo, O. Grulke, C. Hidalgo, B. LaBombard, R. J. Maqueda, P. Scarin, and J. L. Terry, Plasma Phys.: Controlled Fusion **49**, S1 (2007).

[2]S. J. Zweben and R. J. Gould, Nucl. Fusion **25**, 171 (1985).

[3]J. A. Boedo, D. L. Rudakov, R. A. Moyer, G. R. McKee, R. J. Colchin, M. J. Schaffer, P. G. Stangeby, W. P. West, S. L. Allen, T. E. Evans *et al.*, Phys. Plasmas **10**, 1670 (2003).

[4]P. Devynck, J. Brotankova, P. Peleman, M. Spolaore, H. Figueiredo, M. Hron, G. Kirnev, E. Martines, J. Stockel, G. Van Oost, and V. Weinzettl, Phys. Plasmas **13**, 102505 (2006).

[5]N. Fedorczak, J. P. Gunn, J.-Y. Pascal, P. Ghendrih, G. van Oost, P. Monier-Garbet, and G. R. Tynan, Phys. Plasmas **19**, 072314 (2012).

[6]G. R. McKee, R. J. Fonck, M. W. Shafer, I. U. Uzan-Kaymak, and Z. Yan, Rev. Sci. Instrum. **81**, 10D741 (2010).

[7]Y. Sechrest, D. Smith, D. P. Stotler, T. Munsat, and S. J. Zweben, Phys. Plasmas **22**, 052310 (2015).

[8]D. R. Smith, R. J. Fonck, G. R. McKee, D. S. Thompson, R. E. Bell, A. Diallo, W. Guttenfelder, S. M. Kaye, B. P. LeBlanc, and M. Podesta, Phys. Plasmas **20**, 055903 (2013).

[9]M. F. Fox, A. R. Field, F. van Wyk, Y-c. Ghim, and A. A. Schekochihin, and the Mast Team. Plasma Phys. Controlled Fusion **59**, 044008 (2017).

[10]M. F. Fox, F. van Wyk, A. R. Field, Y-c. Ghim, F. I. Parra, and A. A. Schekochihin, and the MAST Team. Plasma Phys. Controlled Fusion **59**, 034002 (2016).

[11]S. J. Zweben, J. L. Terry, M. Agostini, W. M. Davis, A. Diallo, R. A. Ellis, T. Golfinopoulos, O. Grulke, J. W. Hughes, B. LaBombard, M. Landreman, J. R. Myra, D. C. Pace, and D. P. Stotler, Phys. Plasmas **20**, 072503 (2013).

[12]O. Grulke, J. L. Terry, I. Cziegler, B. LaBombard, and O. E. Garcia, Nucl. Fusion **54**, 043012 (2014).

[13]H. Q. Wang, G. S. Xu, B. N. Wan, S. Y. Ding, H. Y. Guo, L. M. Shao, S. C. Liu, X. Q. Xu, E. Wang, N. Yan *et al.*, Phys. Rev. Lett. **112**, 185004 (2014).

[14]S. J. Zweben, W. M. Davis, S. M. Kaye, J. R. Myra, R. E. Bell, B. P. LeBlanc, R. J. Maqueda, T. Munsat, S. A. Sabbagh, Y. Sechrest, and D. P. Stotler, and the NSTX Team. Nucl. Fusion **55**, 093035 (2015).

[15]S. J. Zweben, J. R. Myra, W. M. Davis, D. A. D'Ippolito, T. K. Gray, S. M. Kaye, B. P. LeBlanc, R. J. Maqueda, D. A. Russell, and D. P. Stotler, and the NSTX-U Team. Plasma Phys. Controlled Fusion **58**, 044007 (2016).

[16]I. Shesterikov, Y. Xu, G. R. Tynan, P. H. Diamond, S. Jachmich, P. Dumortier, M. Vergote, M. Van Schoor, and G. Van Oost, and TEXTOR Team. Phys. Rev. Lett. **111**, 055006 (2013).

[17]G. Fuchert, G. Birkenmeier, M. Ramisch, and U. Stroh, Plasma Phys. Controlled Fusion **58**, 054005 (2016).

[18]T. A. Carter and J. E. Maggs, Phys. Plasmas **16**, 012304 (2009).

[19]D. A. Schaffner, T. A. Carter, G. D. Rossi, D. S. Guice, J. E. Maggs, S. Vincena, and B. Friedman, Phys. Plasmas **20**, 055907 (2013).

[20]S. C. Thakur, C. Brandt, L. Cui, J. J. Gosselin, A. D. Light, and G. R. Tynan, Plasma Sources Sci. Technol. **23**, 044006 (2014).

[21]M. Baquero-Ruiz, F. Avino, O. Chellai, A. Fasoli, I. Furno, R. Jacquier, F. Manke, and S. Patrick, Rev. Sci. Instrum. **87**, 113504 (2016).

[22]H. Yinghua, Y. Yi, X. Xiaoyuan, W. Yizhi, L. Wandong, Y. Changxuan, Q. Hong, and L. Ding, Plasma Sci. Technol. **15**, 738 (2013).

[23]G. Birkenmeier, M. Ramisch, G. Fuchert, A. Kohn, B. Nold, and U. Stroh, Plasma Phys. Controlled Fusion **55**, 015003 (2013).

[24]J. R. Myra, D. A. Russell, and S. J. Zweben, Phys. Plasmas **23**, 112502 (2016).

[25]F. D. Halpern, J. L. Terry, S. J. Zweben, B. LaBombard, M. Podesta, and P. Ricci, Plasma Phys. Controlled Fusion **57**, 054005 (2015).

[26]F. Militello, N. R. Walkden, T. Farley, W. A. Gracias, J. Olsen, F. Riva, L. Easy, N. Fedorczak, I. Lupelli, J. Madsen *et al.*, Plasma Phys. Controlled Fusion **58**, 105002 (2016).

[27]H. S. Xie, Y. Xiao, and Z. Lin, Phys. Rev. Lett. **118**, 095001 (2017).

[28]R. M. Churchill, C. S. Chang, S. Ku, and J. Dominski, Plasma Phys. Control. Fusion **59**, 105014 (2017).

[29]S. M. Kaye, T. Abrams, J.-W. Ahn, J. P. Allain, R. Andre, D. Andruczyk, R. Barchfeld, D. Battaglia, A. Bhattacharjee, F. Bedoya *et al.*, Nucl. Fusion **55**, 104002 (2015).

[30]S. J. Zweben, J. L. Terry, D. P. Stotler, and R. J. Maqueda, Rev. Sci. Instrum. **88**, 041101 (2017).

[31]I. Shesterikov, Y. Xu, M. Berte, P. Dumortier, M. Van Schoor, M. Vergote, B. Schweer, and G. Van Oost, Rev. Sci. Instrum. **84**, 053501 (2013).

[32]B. Cao, D. P. Stotler, S. J. Zweben, M. Bell, A. Diallo, and B. LeBlanc, Fusion Sci. Technol. **64**, 29 (2013).

[33]N. Fedorczak, P. Manz, S. C. Thakur, M. Xu, G. R. Tynan, G. S. Xu, and S. C. Liu, Phys. Plasmas **19**, 122302 (2012).

[34]S. J. Zweben, R. J. Maqueda, R. Hager, K. Hallatschek, S. M. Kaye, T. Munsat, F. M. Poli, A. L. Roquemore, Y. Sechrest, and D. P. Stotler, Phys. Plasmas **17**, 102502 (2010).

[35]J. R. Myra, W. M. Davis, D. A. D'Ippolito, B. LaBombard, D. A. Russell, J. L. Terry, and S. J. Zweben, Nucl. Fusion **53**, 073013 (2013).

[36]Y. Sechrest, T. Munsat, D. J. Battaglia, and S. J. Zweben, Nucl. Fusion **52**, 123009 (2012).

[37]O. E. Garcia, Phys. Rev. Lett. **108**, 265001 (2012).

[38]O. E. Garcia, R. Kube, A. Theodorsen, and H. L. Pécseli, Phys. Plasmas **23**, 052308 (2016).

[39]D. P. Stotler, B. LaBombard, J. L. Terry, and S. J. Zweben, J. Nucl. Mater. **313-316**, 1066 (2003).

[40]E. De la Cal and the TJ-II Team, Nucl. Fusion **56**, 106031 (2016).

[41]C. Wersal and P. Ricci, Nucl. Fusion **57**, 116018 (2017).